

General Disclaimer

One or more of the Following Statements may affect this Document

- This document has been reproduced from the best copy furnished by the organizational source. It is being released in the interest of making available as much information as possible.
- This document may contain data, which exceeds the sheet parameters. It was furnished in this condition by the organizational source and is the best copy available.
- This document may contain tone-on-tone or color graphs, charts and/or pictures, which have been reproduced in black and white.
- This document is paginated as submitted by the original source.
- Portions of this document are not fully legible due to the historical nature of some of the material. However, it is the best reproduction available from the original submission.

NASA Contractor Report 174739

(NASA-CR-174739) HIGH TEMPERATURE LOW-CYCLE
FATIGUE MECHANISMS IN SINGLE CRYSTALS OF
NICKEL-BASED SUPERALLOY MAR-M 200 Final
Report (Cincinnati Univ.) 59 p
HC A04/MF A01

N85-12130

Unclas
24449

CSCL 11F G3/26

High Temperature Low-Cycle Fatigue Mechanisms in Single Crystals of
Nickel-Based Superalloy Mar-M 200

Walter W. Milligan and N. Jayaraman

University of Cincinnati
Cincinnati, Ohio

October 1984



Prepared for

NATIONAL AERONAUTICS AND SPACE ADMINISTRATION
Lewis Research Center
Under Grant NSG 3-506

TABLE OF CONTENTS

	<u>Page</u>
Summary	1
Introduction	2
Review of the Literature	3
Experimental Procedure	7
Mechanical Testing	7
Laboratory Evaluation	8
Results and Discussion	9
Results - 760° C	9
Discussion - 760° C	11
Results - 870° C	14
Discussion - 870° C	15
Concluding Remarks	18
References	19
Tables and Figures	20
Appendix - Dislocation Analysis	54

**"High Temperature Low-Cycle Fatigue Mechanisms in Single
Crystals of Nickel Based Superalloy MAR-M 200"**

by

W. W. Milligan and N. Jayaraman
University of Cincinnati

Isothermal low-cycle fatigue (LCF) experiments were conducted on MAR-M 200 single crystal specimens over a range of crystallographic orientations under conditions of controlled cyclic plastic strain. Experiments were run at 760°C and at 870°C. The most significant finding was that LCF life was very orientation dependent and that the effects of orientation are highly influenced by temperature. Extensive transmission electron microscopy studies showed that at 760°C, slip was active on octahedral systems only, and the life results were very consistent with first principal Schmid's laws. At 870°C, however, both octahedral and cubic slip systems were active. The effect of orientation on LCF lives at 870°C could only be understood in terms of time dependent (creep) behavior. The impact of this work is that LCF behavior of single crystal superalloy systems in general will show profound changes over critical usage temperature ranges, and the cyclic parameters most suitable for use in predicting LCF life change.

INTRODUCTION

Material

Mar-M 200 is a nickel-based superalloy developed by Pratt and Whitney Aircraft in the mid 1960's for turbine blade applications. It represents the first generation of materials identified for potential application in the directionally solidified and single crystal forms. The composition and microstructural characteristics are outlined in Figure 1.

The alloy consists of four basic phases¹: The γ matrix, which is a disordered FCC structure containing mostly Ni, Cr, Co, W, and Fe; The γ' precipitate, which is coherent with the matrix. It is an ordered precipitate of the $L1_2$ structure, consisting basically of $Ni_3(Al, Ti, Cb)$; And MC and $M_{23}C_6$ carbides. MC is rich in Ti and W, while $M_{23}C_6$ is rich in Cr.

The specimens were heat treated as follows: Solutionized at 1230°C for 4 hrs, argon quenched, and aged at 870°C for 32 hrs. The resulting microstructure (Figure 2) consisted of a duplex γ' structure containing large, primary γ' which was present from the melt, and finer, secondary γ' which was precipitated during heat treatment.

Due to slow solidification rates in the single crystal growth process, the structure was highly segregated (dendritic). (Figure 3). The dendrite cores (which are reported to be rich in W and Co) contained a smaller average γ' size, and a smaller volume fraction of γ' . The interdendritic areas (which are reported to be rich in Cr, Ti, Ni, and C) contained a larger average γ' size, as well as a larger volume fraction of γ' . (Figure 2). The interdendritic regions also contained MC carbides and "patchy" γ' .

Transmission Electron Microscopy revealed a network of dislocations

at the γ/γ' interface, as well as sub-microscopic carbides in the interdendritic regions. (Figures 4,5).

Review of the Literature

Single crystals are being considered for blade applications because of the lack of grain boundaries, which are extremely weak in creep and fatigue at elevated temperatures. However, single crystals have several inherent disadvantages. One of the strongest disadvantages is that the physical and mechanical properties are anisotropic, and therefore blade performance will vary with crystallographic orientation. The main objective of this study was to determine the effect of tensile axis orientation on the high temperature low cycle fatigue behavior of the alloy.

A brief review of the mechanical behavior and fatigue mechanisms pertinent to this study is presented below.

Since the alloy is composed of approximately 60 Volume % γ' , the mechanical behavior of the γ' phase should be related to the behavior of the alloy. Lall, Chin and Pope² have studied the high temperature mechanical behavior of single crystals of $\text{Ni}_3(\text{Al,Cb}) \gamma'$. They and other investigators have found that the plastic flow characteristics of γ' are controlled by two slip systems. The flow stress rises from its room temperature value to some maximum value at an intermediate temperature, then drops off dramatically at higher temperatures. Below the maximum strength temperature, the predominant slip system is the classical $\langle 110 \rangle \{111\}$ octahedral system. Above the maximum strength temperature, slip begins to occur preferentially in the $\langle 110 \rangle \{100\}$ system (referred to as cube slip). The reason for the increase in flow stress with increasing temperature has been given as

a thermally activated cross slip process from $\langle 110 \rangle \{111\}$ to $\langle 110 \rangle \{100\}$, resulting in dislocation pinning. At higher temperatures, these sessile dislocations begin to slip on the cube planes. They also found a correlation between tensile axis orientation and the temperature of the maximum flow stress.

Ezz and Pope^{3,4} have also studied the asymmetry of the tensile vs. compressive flow stresses in the same alloy. They have reported a strong relationship between orientation and the asymmetry of the tensile/compressive flow stresses up to 927°C. Also, the degree of asymmetry increased with increasing temperature.

Copeley and Kear⁵ studied the flow stress characteristics of off-stoichiometric Ni₃Al γ' single crystals. They noted the same type of behavior, and also attributed it to the octahedral/cube slip combination. They also observed an orientation dependence of the maximum flow stress temperature. It was found to be 815°C (1500°F) for orientations near (001), 760°C (1400°F) for orientations near (011), and 649°C (1200°F) for orientations near (111). In the same study, they compared the flow stress characteristics of the (001) oriented γ' with the flow stress characteristics of (001) oriented single crystals of Mar-M 200. They found that 815°C (1500°F) corresponded to both the maximum flow stress for the γ' and the peak in the yield stress curve of the cube oriented Mar-M 200, thus indicating a possible relationship.

Kear and Piarcey¹ studied the tensile properties of single crystals of Mar-M 200. They showed that the plastic flow behavior of the alloy is strongly dependent on orientation up to 760°C, but is fairly constant in the range from 760°C to 982°C. At low temperatures, slip on octahedral planes

is dominant. In "single slip" orientations (in the middle of the stereographic triangle, where only one octahedral plane is favorably oriented for slip), yield strength is low and ductility is high. In "multiple slip" orientations (near the (001), (011), and (111) poles, where more than one octahedral plane is favorably oriented for slip), a higher degree of strain hardening leads to higher strengths and reduced ductility. At higher temperatures, they presented evidence for cube slip and octahedral slip occurring in the γ' , which tended to reduce the effect of orientation.

Although tensile deformation modes are fairly well documented and understood, high temperature fatigue is much more complex. Such factors as the effects of repeated loading, mean stresses, microstructural defects, environmental degradation, phase instabilities, and the possibility of creep damage must all be considered.

There are two basic types of plastic deformation in low cycle fatigue of nickel based superalloy single crystals^{7,8} (excluding creep). At low temperatures, high frequencies, low applied stresses, and low stacking fault energies, planar slip is favored. Planar slip usually leads to the formation of slip bands and crystallographic (Stage I) cracking. Conversely, low frequencies, high applied stresses, high stacking fault energies, and most importantly temperatures in excess of 40% of the homologous melting temperature favor cross slip and a wavy, homogeneous deformation structure. Wavy slip favors non-crystallographic (Stage II) cracking perpendicular to the tensile axis.

Wells, Leverant, Sullivan, and Gell^{7,8,9} investigated the low cycle fatigue behavior of carbide containing and carbide free single crystals of Mar-M 200 in near (001) orientations. They found that planar slip

dominated at room temperature and 760°C, while wavy slip dominated at 927°C. Cracks were initiated at carbides in the carbide containing material, and at sub-surface micropores in the carbide free material.

Leverant and Gell¹⁰ studied the low cycle fatigue behavior of near (001) single crystals between 760°C and 982°C. They confirmed the observations concerning planar and wavy slip, and Stage I and Stage II cracking that were discussed above. They also determined that at low frequencies at 843°C and 927°C, creep plays an important role in controlling the fatigue behavior. This complicates the evaluation even further.

Earlier, Leverant, Kear, et. al.^{11,12,13} studied creep mechanisms in single crystals of Mar-M 200 at 760°C and 857°C. They found that at 760°C, γ' shear is controlled by $\langle 112 \rangle \{111\}$ slip in primary creep, but is controlled by the $\langle 110 \rangle \{111\}$ system in steady state creep. Moreover, it was found that strain hardening due to intersecting slip was necessary to obtain the transformation from primary to steady state creep. At 857°C, both primary and steady state creep were controlled by the $\langle 110 \rangle \{111\}$ system.

Obviously, the high temperature low cycle fatigue behavior of the alloy is complex, and interactions between different mechanisms are not fully understood.

EXPERIMENTAL PROCEDURE

Mechanical Testing

Low cycle fatigue tests were conducted over the summer of 1983 at NASA-Lewis Research Center, Cleveland, Ohio.

The test facility consisted of an MTS Closed Loop Servohydraulic Structure Test System. The load cell was calibrated by using a tool steel specimen with a known elastic modulus and a strain gage system.

During testing, strain was measured by a spring loaded, quartz rod extensometer which is shown schematically in Figure 6. The extensometer was constructed by applying strain gages to the top and bottom of a spring steel flexure, which was attached by an aluminum frame to the quartz probes. The resulting four-arm, fully active wheatstone bridge was calibrated by a precision micrometer, and found to produce a linearly varying signal in the displacement range of interest. Strains and strain ranges were measured by a high resolution digital oscilloscope.

The specimens were heated by means of a high frequency induction furnace. By means of a calibration specimen containing six thermocouples at different locations, and an optical pyrometer, it was determined that the temperature gradient in the gage length (radially and longitudinally) was less than $\pm 2^{\circ}\text{C}$. Temperature was controlled manually with the aid of a thermocouple in the shoulder area of the specimen, which resulted in a temperature variation of $\pm 7^{\circ}\text{C}$. Temperature was recorded continuously on a strip chart plotter.

Twenty three high temperature low cycle fatigue tests were conducted, 14 at 760°C and 9 at 870°C . The specimens were hollow cylinders, as illustrated in Figure 7. Testing was conducted in the longitudinal strain

controlled mode, in a fully reversed tension/compression strain cycle. The cyclic frequency was 0.1 Hz. The plastic strain range was held constant, while the orientation of the tensile axis varied from specimen to specimen. All but two of the specimens were cycled to failure.

Plots of stress vs. time, strain vs. time, and temperature vs. time were continuously recorded, and the stress/strain hysteresis loop was recorded intermittently.

Laboratory Evaluation

Specimen orientations were determined prior to testing by the Laue Back Reflection Technique.

Metallographic and fractographic studies were conducted using a Leitz metallograph and an Amray 1200 SEM with EDS capability.

Thin foils were prepared for Transmission Electron Microscopy by grinding to 0.075 mm thick, ion milling, and finally twin-jet electropolishing.

Foils were studied on a JEOL JEM 200 TEM operated at 200 kV.

RESULTS and DISCUSSION

Specimen orientations are presented in Table I and Figure 8. Room temperature and elevated temperature elastic moduli are presented in Tables II, III. The anisotropy is clearly evident, as the room temperature modulus of elasticity varied from 90 GPa to 220 GPa with different orientations.

Results and a discussion of the fatigue behavior are divided into two sections, based on test temperature.

Results-760°C

Nine tests were conducted at a nominal plastic strain range ($\Delta\epsilon_p$) of 0.1%, and four tests were conducted at higher plastic strain ranges. Experimental parameters are plotted vs. orientation in Figure 9.

As these figures illustrate, when the $\Delta\epsilon_p$ was held constant but the tensile axis orientation was changed, other test parameters (total strain range ($\Delta\epsilon_t$), stress range ($\Delta\sigma$), and most importantly cyclic life (N_f)) varied significantly. Several trends can be clearly identified:

Orientations near the poles (especially (001) and (111)) resulted in high stress ranges and low lives. Based on Schmid's Law criteria, these orientations are referred to as "multiple slip" orientations, because more than one octahedral plane is favorably oriented for slip. Orientations in the middle of the stereographic triangle (away from the poles) resulted in lower stress ranges and higher lives. These orientations are referred to as "single slip" orientations, because only one octahedral plane is favorably oriented for slip. Total strain ranges varied independently of these trends, due to the different degrees of elastic strain caused by

different elastic moduli.

The initial cyclic behavior was also dependent on orientation. Orientations near (001) and (111) strain hardened rapidly and stabilized early in the test, while single slip orientations and orientations near (011) hardened much less rapidly, and in some cases did not completely stabilize.

A detailed metallurgical study was undertaken to determine the mechanisms responsible for the observed behavior.

It was established through SEM fractography and optical metallography that the mechanisms of crack initiation and propagation were essentially independent of orientation. Every specimen showed strong evidence of multiple crack initiation at surface connected and sub-surface micropores. (Figures 11-13). Some evidence of Stage I crack initiation involving carbides (Figure 14) and initiation due to "cracked" carbides (Figure 15) was found metallographically, but the major "crack initiator" appeared to be microporosity. Crack propagation was observed to be in the Stage II mode (perpendicular to the tensile axis). Final tensile failure occurred by a combination of crystallographic cracking along shear planes and interdendritic tearing. (Figure 16).

One orientation effect was observed optically: single slip orientations and orientations near (011) had obvious slip traces on the specimen surface. (Figures 17, 11). Orientations near (001) and (111) showed no evidence of these slip traces. It was determined that the slip traces corresponded to the primary octahedral shear planes. The fatigue cracks always initiated at the apices of the slip trace ellipses, which corresponded to the region where the normal stress, which opens the crack and facilitates early

propagation, was at a maximum. (Figure 18).

Over half of the tested specimens were evaluated by Transmission Electron Microscopy. It was confirmed that the majority of the dislocations present in the single slip orientations did lie on the primary octahedral shear plane, and many of these dislocations were present in a parallel array of dislocation bands. (Figure 19). Most of these dislocations were of the type $a/2[\bar{1}01](111)$. (Details of the dislocation analysis technique used to determine the burgers vector and the slip plane are presented in Appendix A). Although there were some dislocations present in the γ' , the majority of the dislocations appeared to be in the matrix or at the γ/γ' interface. Several dislocations of the type $a/2[\bar{1}01](010)$ (Cube planes) were observed in the γ' , but they did not appear to be very numerous. Also, they did not appear to be shearing the γ' . More work is being done to confirm these observations.

In the multiple slip orientations, slip occurred on more than one octahedral plane, as predicted by Schmid's Law. Intersecting slip bands were observed. (Figures 20, 21).

Discussion-760°C

The relationships between fatigue behavior, cyclic life, and orientation can be explained very well by Schmid's Law at this temperature. Single slip orientations plastically deformed by dislocation glide on a single (111) plane. This resulted in relatively easy glide and a high degree of slip reversibility. These factors combined to form the optimum conditions for maximum low cycle fatigue life: A minimum in dislocation/dislocation interactions, resulting in the minimum amount of strain hardening, the highest degree of ductility, and therefore the highest fatigue lives. Also, the small degree of strain hardening resulted in small stress ranges, which

probably decreased the fatigue crack propagation rates.

Multiple slip orientations plastically deformed by dislocation glide on more than one (111) plane. This resulted in a high degree of strain hardening caused by dislocation/dislocation interactions on intersecting slip planes. These factors lead to the worst possible conditions for fatigue life: A minimum degree of slip reversibility, a large amount of strain hardening, low ductility, and therefore low fatigue lives. The large degree of strain hardening also resulted in high stress ranges, which probably increased the fatigue crack propagation rates.

A Coffin-Manson plot was attempted, but N_f varied by more than a factor of 10 for the same nominal $\Delta\epsilon_p$. A plot of $\Delta\epsilon_t$ vs. N_f proved fruitless because of the differences in elastic moduli. The most successful relationship was found to exist between $\Delta\sigma$ and N_f , where most of the data fell within a factor of 2. (Figure 10). This is the case because the stress range is intimately related to orientation, strain hardening, and ductility, as explained above.

The question of optimum tensile axis orientation was investigated. On first glance, it would appear that the single slip orientations were more fatigue resistant than the multiple slip orientations. Closer inspection of the data, however, reveals that this was not necessarily the case:

The controlled variable in these tests was the plastic strain range. Multiple slip orientations have lower ductilities than single slip orientations. Since the ductility is lower, it would be reasonable to assume that the lives would be shorter when the controlled parameter was plastic strain range. However, if the consistent parameter was

total strain range or stress range, the data would seem to indicate that the multiple slip orientations would be far superior. For example, the following is a comparison between a single slip and a multiple slip case:

Specimen	<u>Single Slip</u> FF40	<u>Multiple Slip</u> FF32
Orientation	Middle	(001)
$\Delta\epsilon_p$ (%)	0.069	0.074
$\Delta\epsilon_t$ (%)	0.7 ^c	1.83 [*]
$\Delta\sigma$ (MPa)	1300	1700
Cycles to Failure	550	77

*The (001) orientation has the lowest elastic modulus, which is the main reason for the large total strain range.

On first glance, FF40 appears superior. However, if the controlled variable was total strain range or stress range, this conclusion would change. There are two initial possibilities:

1. Test FF32 at the same total strain range or stress range as FF40. In this case, the (001) specimen would have virtually zero plastic strain, and the life should be very high.
2. Test FF40 at the same total strain range or stress range as FF32. In this case, FF40 would last exactly 1/4 cycle: The ultimate tensile strength would be exceeded on initial loading.

Results-870°C

Eight tests were conducted at a nominal $\Delta\epsilon_p$ of 0.1%. Experimental parameters are plotted vs. orientation in Figure 22.

The fatigue behavior at this temperature was also orientation dependent, but the trends were not the same as they were at 760°C. For the same plastic strain range, orientations near (001) resulted in low stabilized stress ranges and high lives, while orientations near (011) resulted in high stabilized stress ranges and low lives, and orientations between the two (in the middle of the stereographic triangle) exhibited intermediate behavior. No specimens near (111) were available for testing.

The initial cyclic behavior also varied with orientation (Figure 24). Orientations near (001) were cyclically stable, while other orientations cyclically softened. "Single Slip" orientations softened the most, while (011) orientations softened to a lesser degree.

As shown in Figure 25, there was a very good correlation between $\Delta\sigma$ and N_f .

SEM fractography was able to identify a relationship between orientation and crack morphology. Although all cracks initiated at micropores (Figures 25-28) regardless of orientation, the crack propagation mode varied. Orientations near (001) contained distinct, smooth "initiation" zones that exhibited the familiar "clamshell" pattern. (Figure 25). This pattern is typical of low stress propagation. Other orientations exhibited a rougher, more textured fracture surface, which is typical of higher stress propagation. (Figures 26,27). The textured surface

was also observed in the (001) orientations in the later stages of propagation. (Figure 25). No slip traces were observed at 870°C.

Transmission Electron Microscopy revealed a very homogeneous, non-planar deformation structure, which included a high concentration of "wavy" $a/2\langle 110 \rangle$ type dislocations within the γ' . The dislocation structure was not confined to several planes, but was rather present as dislocation loops which lied on many planes. (Figures 29-31). This structure is a result of extensive cross slip and climb¹⁴, and has been documented for Mar-M200 tested in tension at 843°C¹⁴, in creep at 857°C¹⁵, and in low stress fatigue at 843°C¹⁰.

The most significant observation was that the fatigue microstructure appeared to be independent of orientation. Both octahedral and cube plane dislocations were identified within the γ' in all orientations, but the majority of dislocations were non-linear, and were not confined to one or two planes.

Discussion-870°C

In contrast to 760°C, Schmid's Law alone cannot explain the fatigue behavior, based only on octahedral slip. Also, since the equilibrium deformation structure appeared to be independent of orientation, it does not seem likely that orientation dependent cube slip was responsible for the behavior. A mechanism that seems very possible, and is based on orientation dependent creep rates, is discussed below.

It has been shown¹⁴ that at 843°C and at strain rates up to 10 times those used in the present study, the deformation behavior of this alloy is very strain rate dependent. TEM studies showed that the reason for this strain rate dependence (and the primary deformation mechanism) was a time dependent shear of the γ' particles. This shear took place by diffusion assisted glide of "wavy" $a/2\langle 110 \rangle$ dislocations.

Since the microstructure after fatigue in the present study contained a high concentration of "wavy" $a/2\langle 110 \rangle$ within the γ' , it seems reasonable to assume that a time dependent (creep) mechanism was active during fatigue at 870°C. This can help explain the orientation dependence. It has been shown that creep deformation is very orientation dependent in this alloy¹ although a limited number of orientations were tested. Recent work on Ni₃Al γ' single crystals¹⁶ has shown that the minimum creep rate of the (001) orientation was about twice the minimum creep rate of the (011) and (123) orientations.

Taken together, these observations can explain the fatigue behavior. In plastic strain controlled fatigue, a high steady state creep rate would lead to stress relaxation and low stress ranges, because the material is accumulating a large amount of creep strain per cycle. Conversely, a low creep rate would result in less stress relaxation, and therefore higher stress ranges. The observed behavior of the alloy correlates very well with this argument: The near (001) orientation, which had the highest creep rate in the pure γ' , resulted in the lowest

stress ranges; and the (011) orientation, which should have the lowest creep rate of the orientations tested, resulted in the highest stress ranges.

The fatigue lives can also be explained in a manner consistent with the above arguments. The deformation mechanisms and dislocation structures were independent of orientation, but the relative deformation rates (creep vs. plasticity) were not. The net result was a high stress range for the more creep resistant orientations. Since the mechanisms and the plastic strains were independent of orientation, and since the stress ranges correlated very well with life, it could be reasonably assumed that the stress response controlled the life. The fractographic observations support this conclusion. Crack initiation was independent of orientation (at micropores), but the crack morphology was very orientation dependent in the early stages of propagation.

CONCLUDING REMARKS

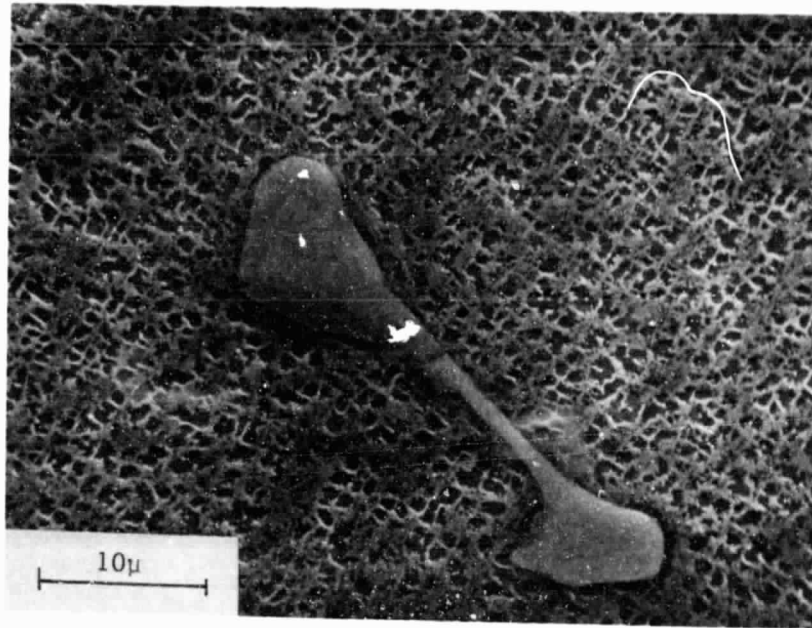
The low cycle fatigue behavior of the alloy under the same frequency and approximate $\Delta\epsilon_p$ was very different at 760°C than at 870°C. At 760°C, planar slip lead to orientation dependent strain hardening and lives. At 870°C, orientation dependent creep rates lead to orientation dependent stress ranges and lives. The ductility at 870°C was much higher, while the strength was lower. In plastic strain control, this resulted in higher lives at the higher temperature. Also, the orientation dependence of life (for the same $\Delta\epsilon_p$) was less pronounced at 870°C, as the life variation was reduced from a factor of 10 at 760°C to a factor of 4 at 870°C.

REFERENCES

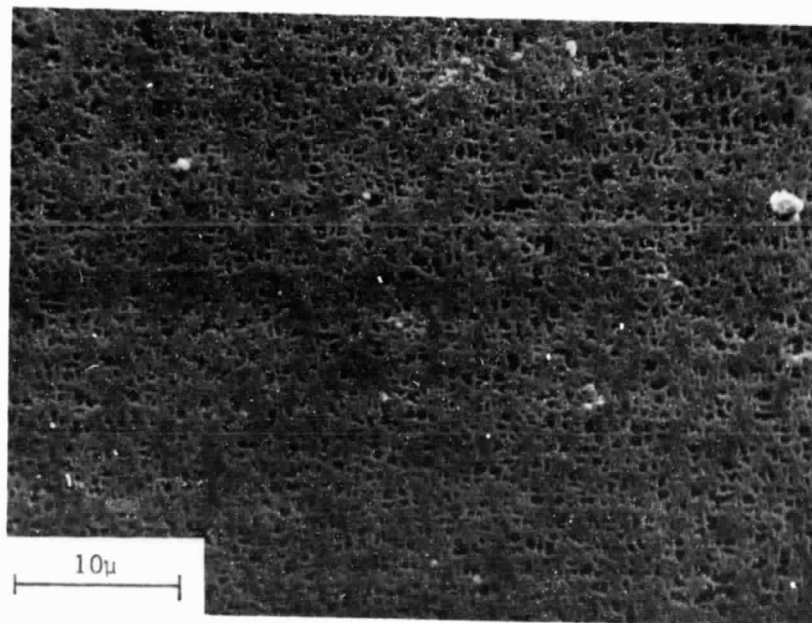
1. B. Kear and B. Pearcey: Trans. TMS-AIME, Vol. 239, August 1967, pp. 1209-1215.
2. C. Lall, S. Chin, and D. Pope: Met. Trans. A, Vol. 10A, Sept. 1979, pp. 1323-1332.
3. S. Ezz, D. Pope, and V. Padair: Acta. Met., Vol. 30, 1982, pp. 921-926.
4. S. Ezz and D. Pope: Scripta Met., Vol. 16, 1982, pp. 117-118.
5. S. Copeley and B. Kear: Trans. TMS-AIME, Vol. 239, July 1967, pp. 977-984.
6. S. Copeley, B. Kear, and G. Rowe: Mater. Sci. Eng., Vol. 10, 1972, pp. 87-92.
7. C. Wells, C. Sullivan, and M. Gell: "Mechanisms of Fatigue in the Creep Range", ASTM STP 495, ASTM, 1971, pp. 61-122.
8. M. Gell and G. Leverant: "Mechanisms of High Temperature Fatigue", ASTM STP 520, ASTM, 1973, pp. 37-67.
9. M. Gell and G. Leverant: "The Effect of Temperature on Fatigue Fracture in a Directionally Solidified Nickel Based Superalloy", 2nd International Conference on Fracture, Brighton, U.K., April 1969.
10. G. Leverant and M. Gell: Met. Trans A, Vol. 6A, Feb. 1975, pp. 367-371.
11. G. Leverant and B. Kear: Met Trans., Vol. 1, Feb. 1970, pp. 491-498.
12. R. Paslay, C. Wells, and G. Leverant: J. Appl. Mech., Sept. 1970, pp. 759-764.
13. G. Leverant, B. Kear, and J. Oblak: Met. Trans., Vol. 4, Jan. 1973, pp. 355-362.
14. G.R. Leverant, M. Gell and S.W. Hopkins: Mater. Sci. Eng., Vol. 8, 1975, pp. 125-133.
15. G.R. Leverant, B.H. Kear, and J.M. Oblak: Met. Trans., Vol. 4, Jan. 1973, pp. 355-362.
16. D.M. Shah: Scripta Met., Vol. 17, 1983, pp.997-1002.

<u>Element</u>	<u>Weight %</u>	<u>Function</u>
Ti	2.05	γ' Formers
Al	5.00	
Cb	1.00	
Cr	9.20	Corrosion Resistance
Co	10.40	γ Solid Solution Strengtheners
W	12.60	
Fe	0.30	
Zr	0.05	Remnants of Polycrystalline Alloy, Where Carbides and Zr, B Were Used to Strengthen Grain Boundaries and Improve Creep Resistance
C	0.15	
B	0.02	
Ni	Bal.	γ Matrix, γ'

Fig. 1. Mar-M 200 alloy composition and microstructural characteristics.



A



B

Fig. 2. SEM micrographs of the as-received microstructure. A) Interdendritic region, showing large, primary γ' and finer, secondary γ' , and an MC carbide. EDS analysis showed the carbide to be rich in W, Ti, and Cb. B) Dendrite core, showing smaller primary γ' size and a smaller volume fraction γ' .

ORIGINAL PAGE IS
OF POOR QUALITY

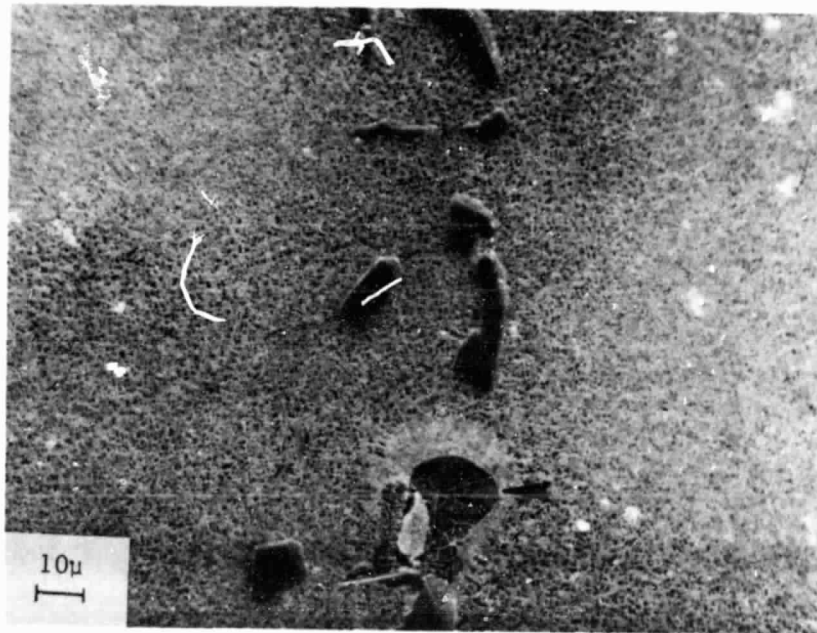


Fig. 3. Lower magnification SEM micrograph illustrating the dendritic segregation. Note the large, "patchy" γ' in the interdendritic region (arrow). Other large particles are MC carbides.

ORIGINAL PAGE IS
OF POOR QUALITY

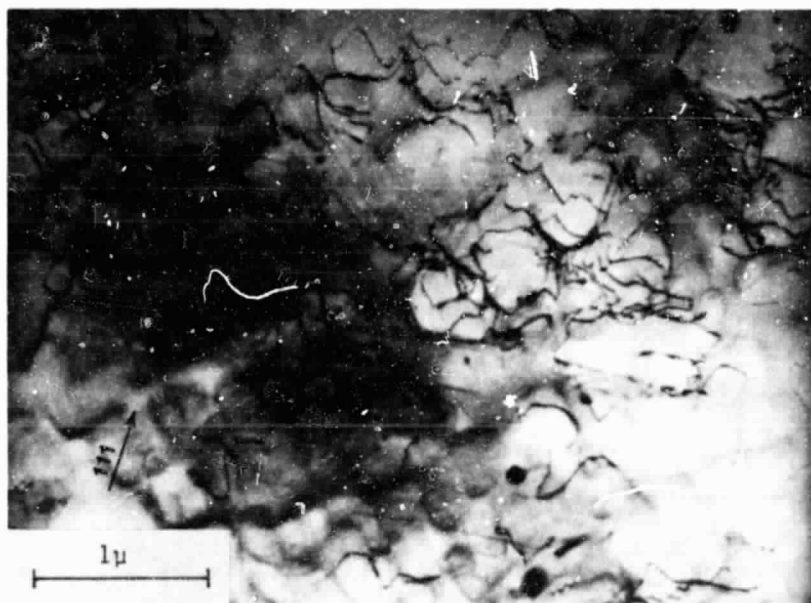
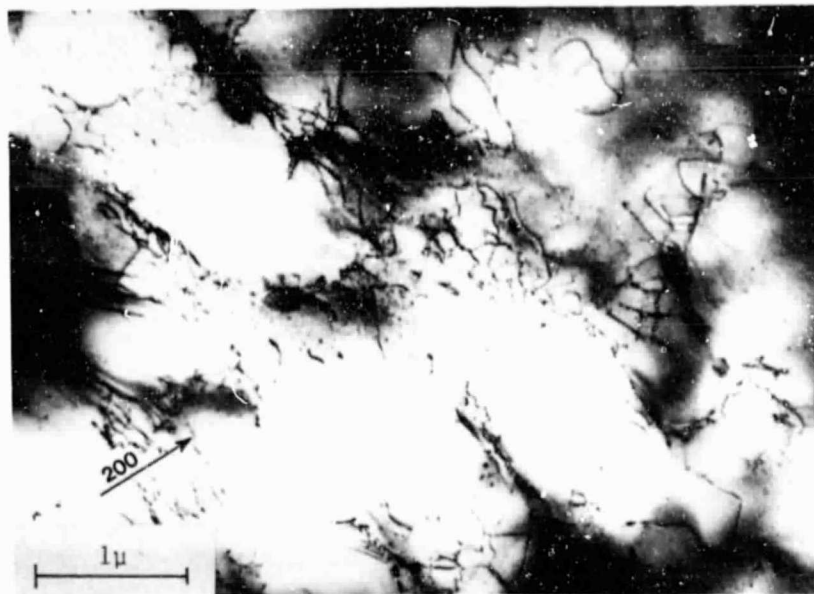
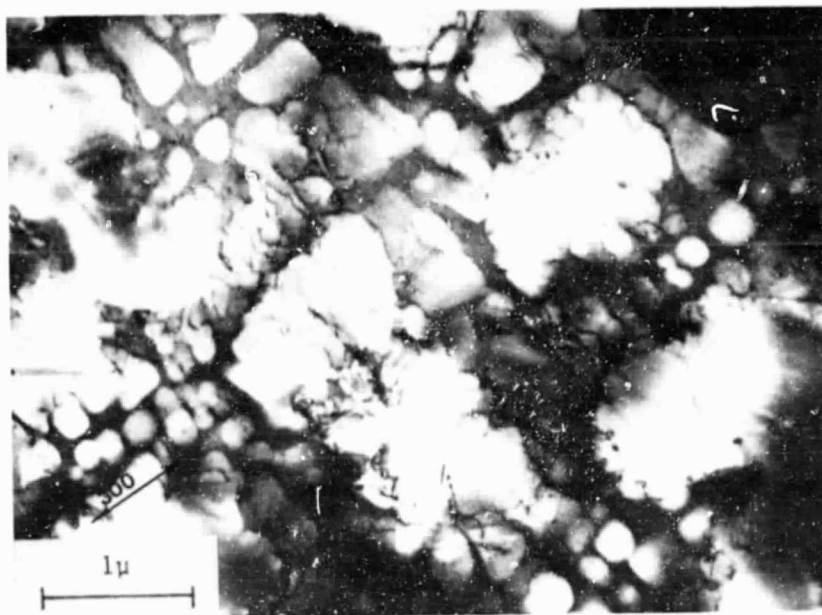


Fig. 4. Bright field (BF) TEM micrograph of the as-received microstructure. Note the interfacial dislocation network and carbides (small dark particles).



A



B

Fig. 5. TEM micrographs of the as-received microstructure. A) BF showing interfacial dislocations. B) Central Dark Field (CDF) showing the bi-modal γ' morphology and interfacial dislocations. (Not same area as 5A).

ORIGINAL PAGE IS
OF POOR QUALITY

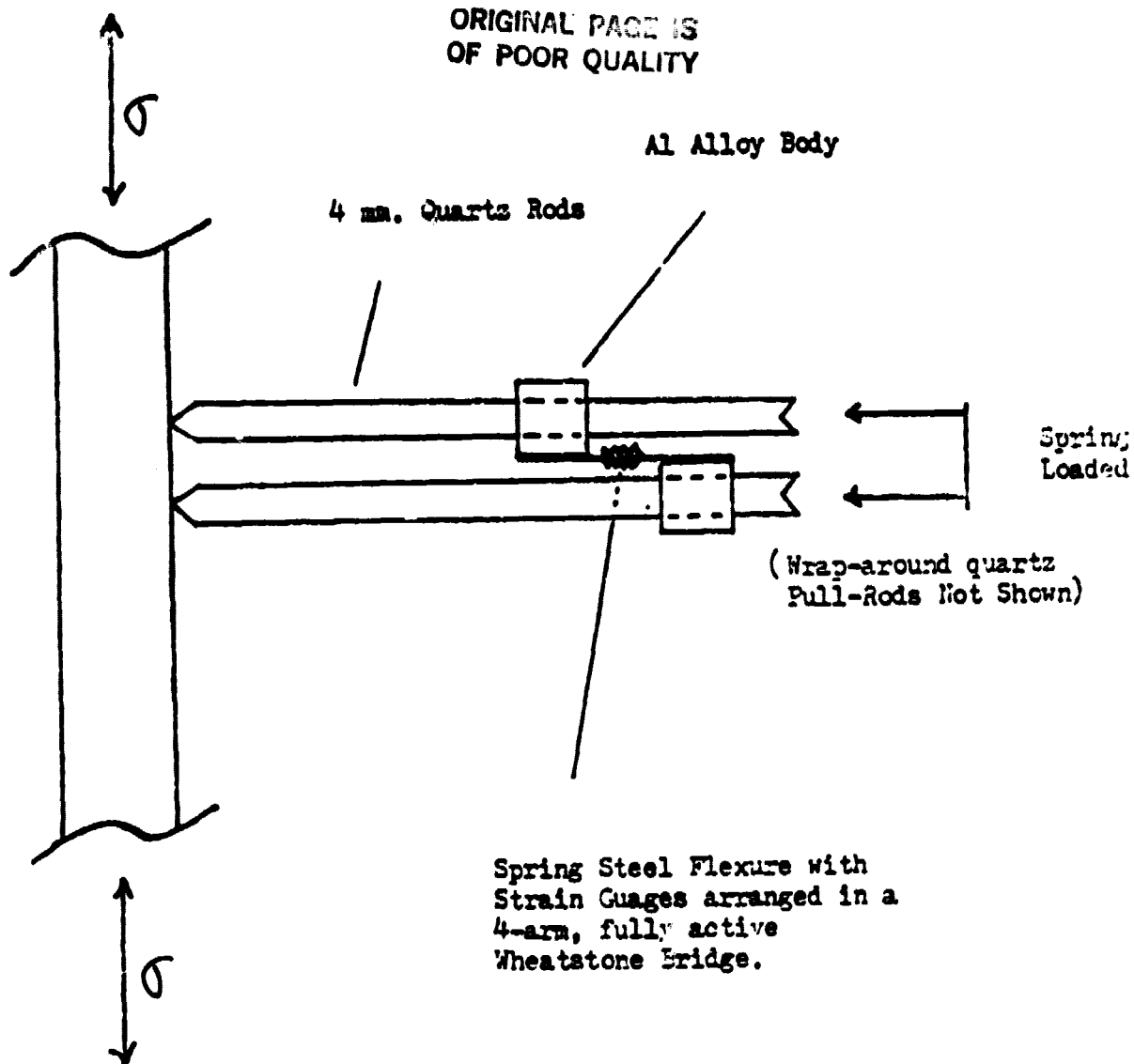


Fig. 6. Schematic of the High Temperature Extensometer

A SURFACES & P.D. OF THREADS
MUST BE CONCENTRIC, SQUARE
& TRUE WITHIN .0005 F.I.R.

✓ 16/ ALL OVER EXCEPT AS NOTED

ORIGINAL PAGE IS
OF POOR QUALITY

SPECIAL NOTE: DIAMETERS MUST BE UNIFORM
ALONG 1.12-1.13 GAGE LENGTH TO WITHIN
.0005

CHAMFER 45° x .03
BOTH ENDS

5/8 - 18 NF - 3
BOTH ENDS

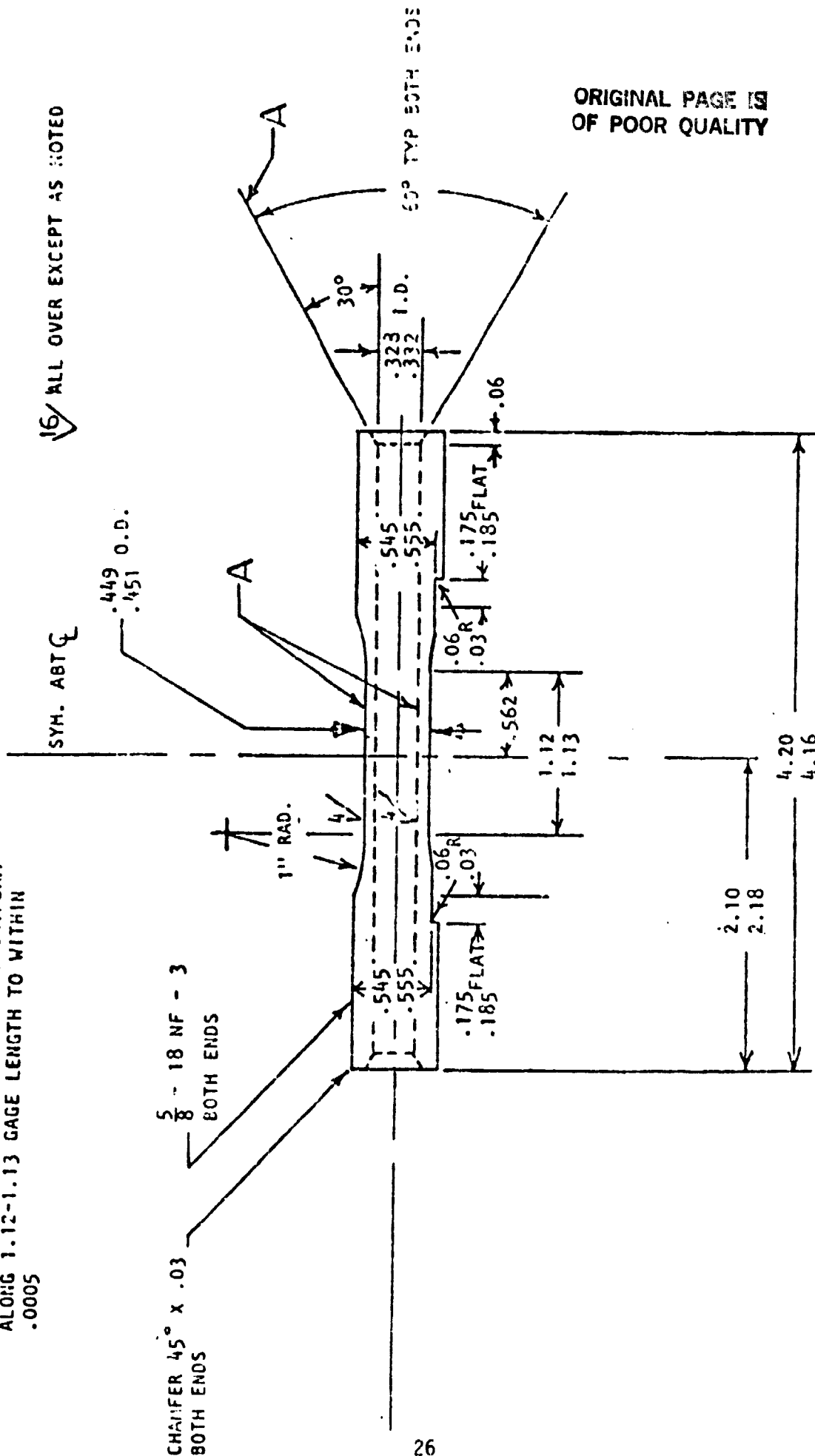


Fig. 7. Specimen Geometry

Table I
Specimen Orientations

Test Temperature	Number	Degrees from		
		<001>	<111>	<011>
750°C	32	4	51	42
	25	5	40	40
	14	40	14	30
	45	44	33	2
	19	38	33	8
	23	17	40	39
	47	18	38	28
	43	27	37	20
	41	27	34	20
	38	24	32	30
	4	36	21	24
	40	46	22	14
	49	45	21	15
	27*	7	50	40
870°C	34	8	48	38
	48	11	45	34
	51	11	45	37
	21	40	36	5
	46	46	28	6
	29	24	39	21
	20	32	27	21
	39	46	25	13
	52*	10	45	38

*Not cycled to failure

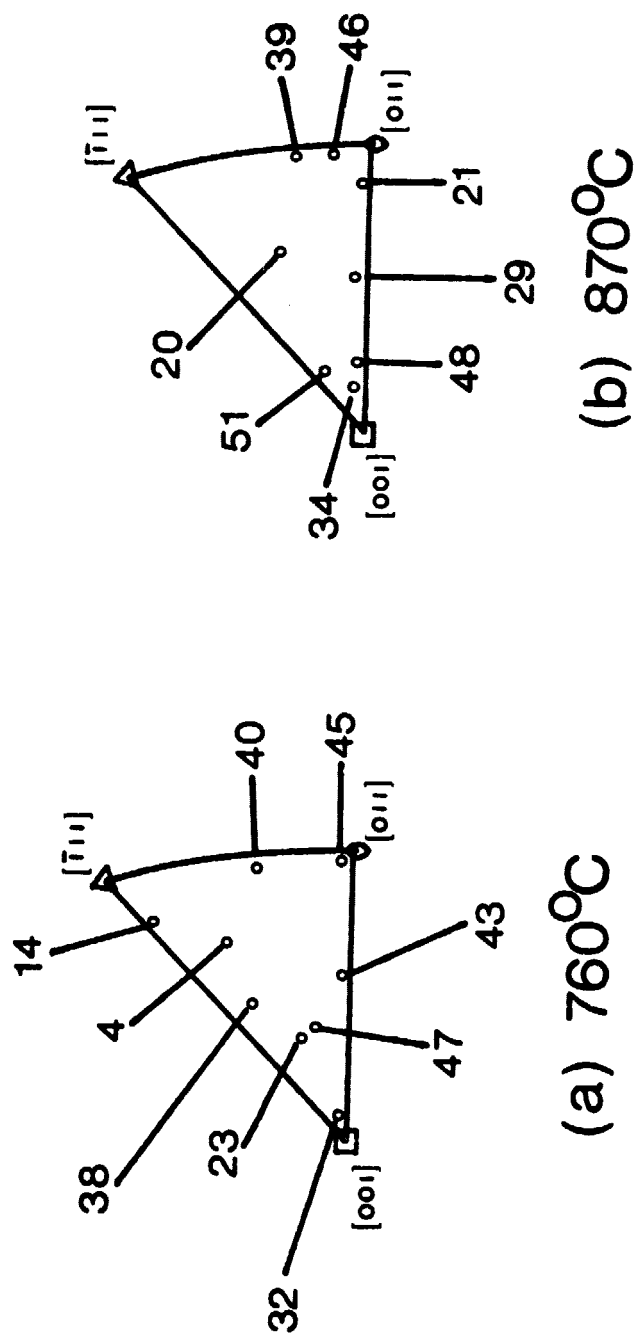


Fig. 8. Tensile axis orientations of the tested specimens (Constant $\Delta\epsilon_p$ only).

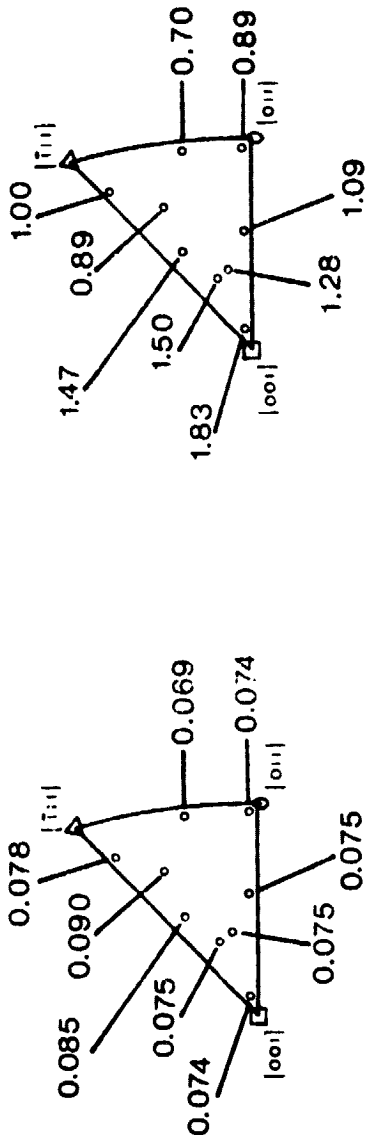
Table II

Experimental Data - 760°C

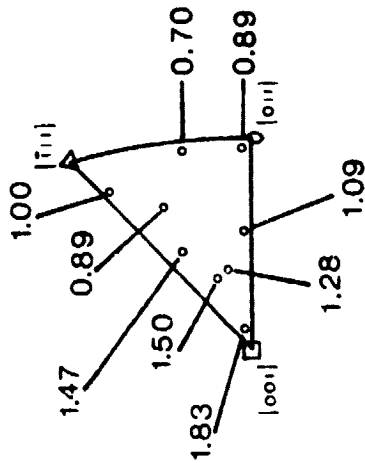
Specimen Number	E (20°C), GPa	E (760°C), GPa	$\Delta\epsilon_p$, %	$\Delta\epsilon_t$, %	$\Delta\sigma$, MPa	σ_m , MPa	N_f^*
32	121	97	0.074	1.83	1700	38	77
25	134	108	0.287	1.91	1760	54	36
14	255	211	0.078	1.00	1940	-23	47
45	239	198	0.074	0.89	1620	-38	137
19	158	121	0.226	1.41	1440	-47	179
23	127	106	0.075	1.50	1520	33	115
47	142	115	0.075	1.28	1400	56	220
43	183	145	0.075	1.09	1480	-22	328
41	158	131	0.246	1.40	1510	-67	100
38	132	102	0.085	1.47	1420	49	310
4	195	203	0.090	0.89	1630	23	452
40	261	205	0.069	0.70	1300	-10	550
49	230	186	0.164	0.95	1480	-19	187

* N_f defined as total failure or a 10% drop in tensile load.

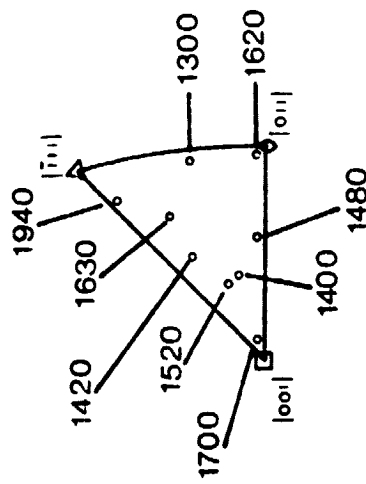
ORIGINAL PAGE IS
OF POOR QUALITY



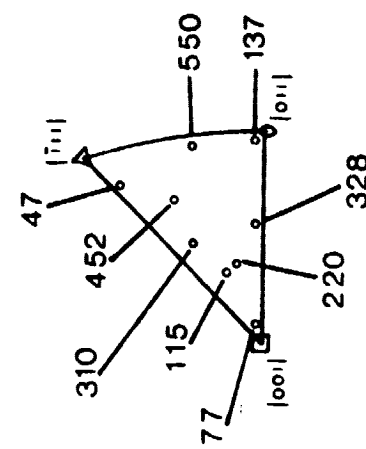
(a) $\Delta\epsilon_p$ [%]



(b) $\Delta\epsilon_t$ [%]



(c) $\Delta\sigma$ [MPa]



(d) N_f

Fig. 9. Experimental data from the 760°C, constant plastic strainrate tests.

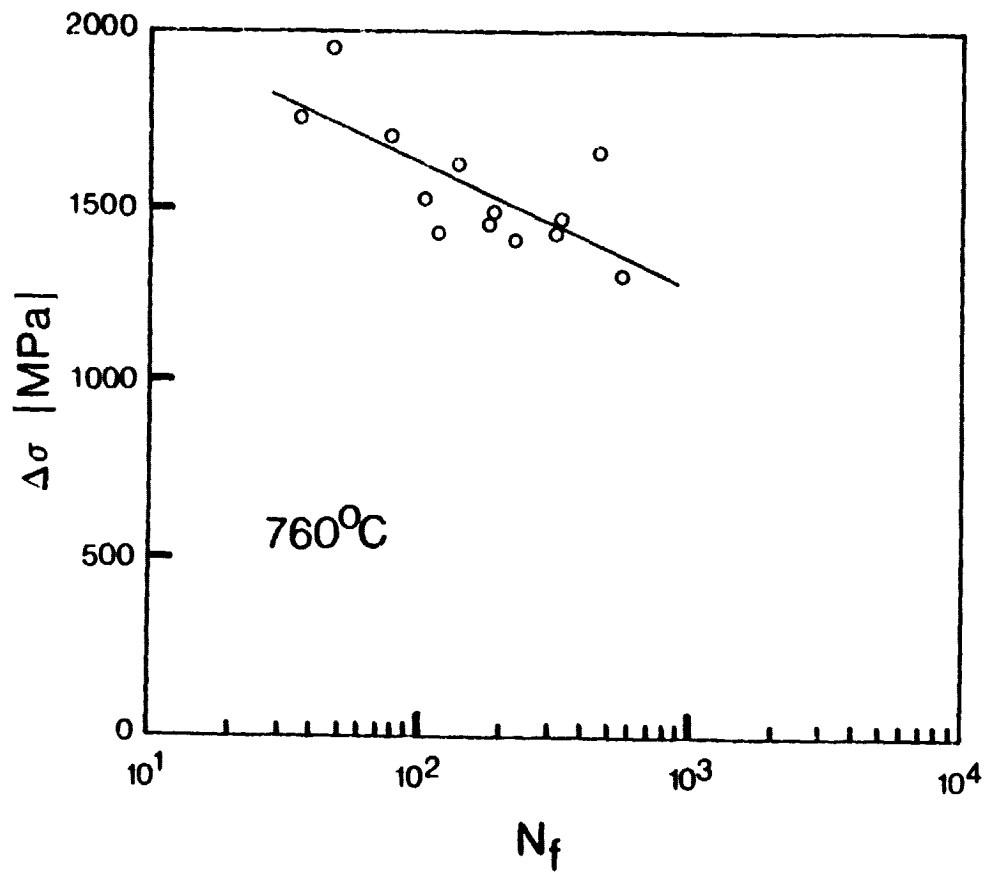
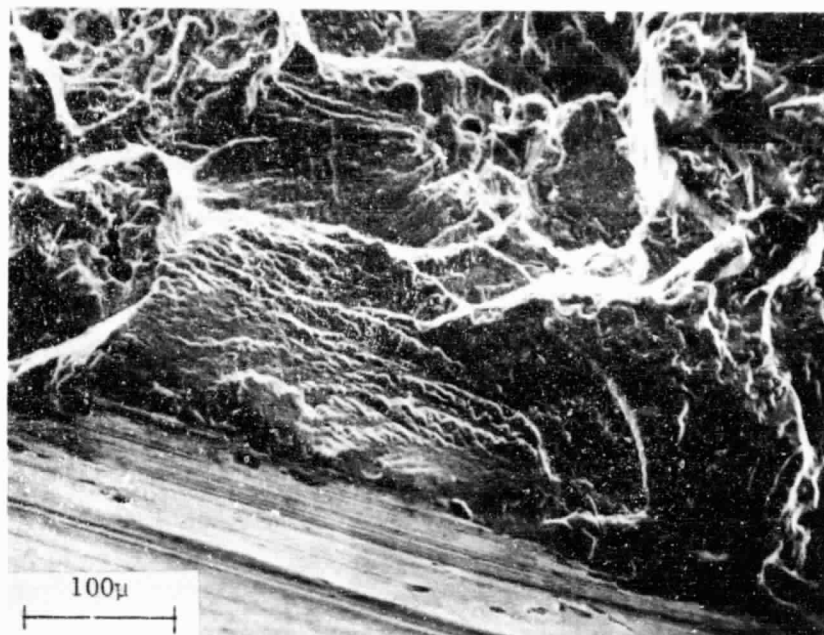
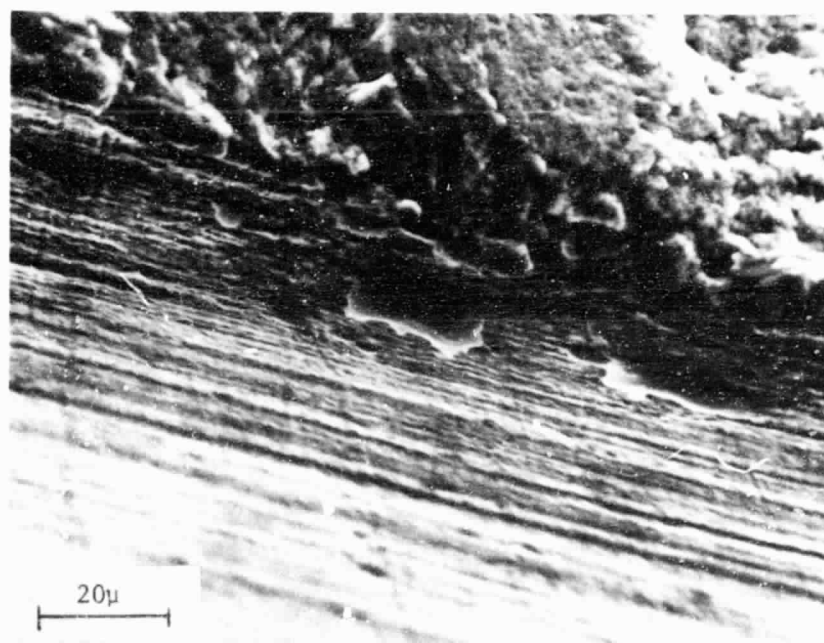


Fig. 10. $\Delta\sigma$ vs. N_f at 760°C .

ORIGINAL PAGE IS
OF POOR QUALITY



A



B

Fig. 11. Increasing magnification SEM fractographs showing microporosity at the crack initiation site. Specimen PF43. Note slip traces on the specimen surface.

ORIGINAL PAGE IS
OF POOR QUALITY

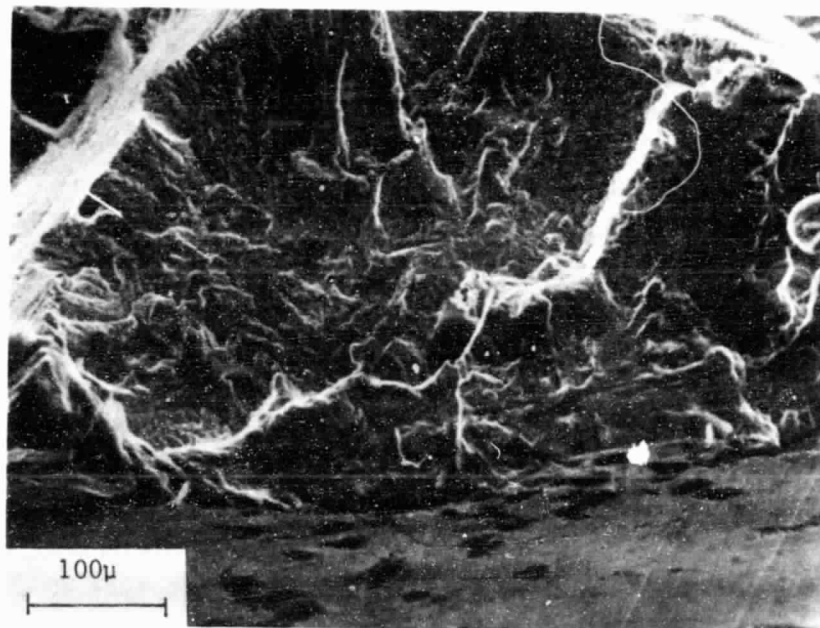
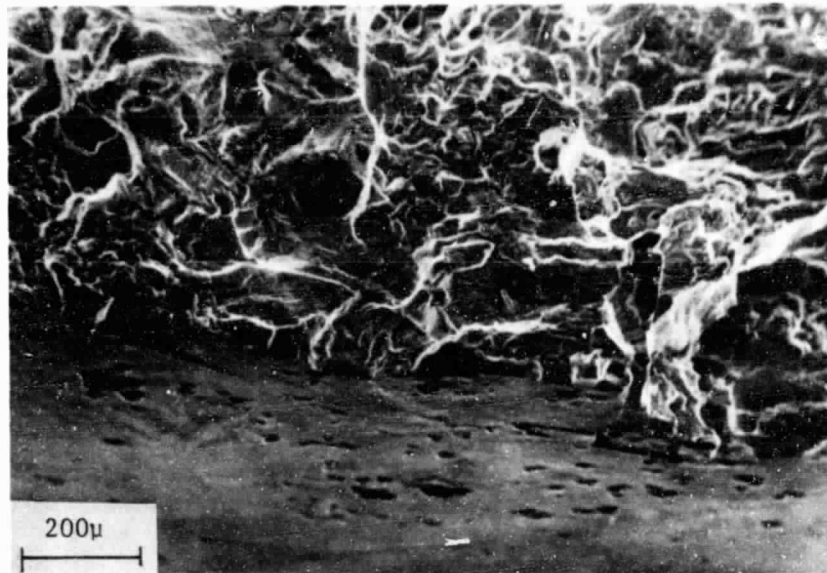
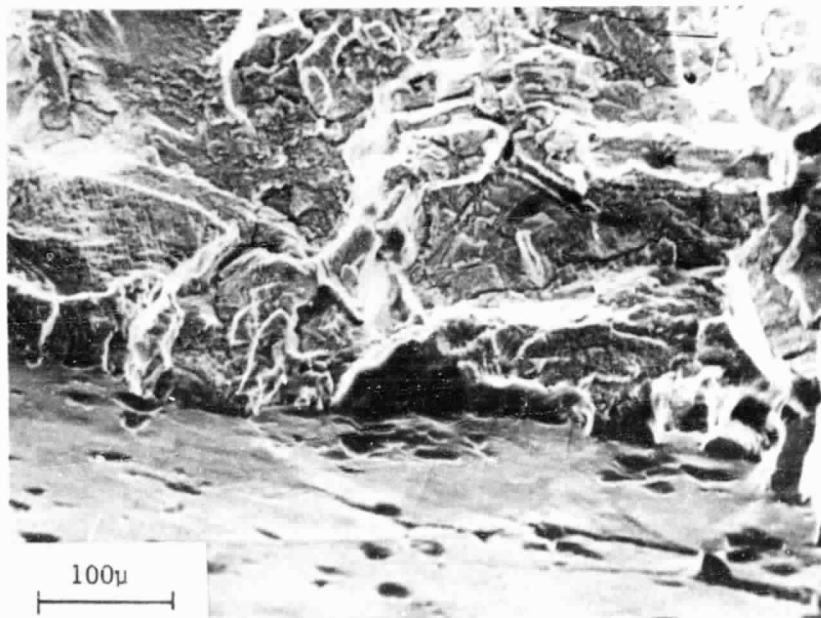


Fig. 12. SEM fractograph showing a high concentration of micropores at the crack initiation site. Specimen FF38.

ORIGINAL PAGE IS
OF POOR QUALITY



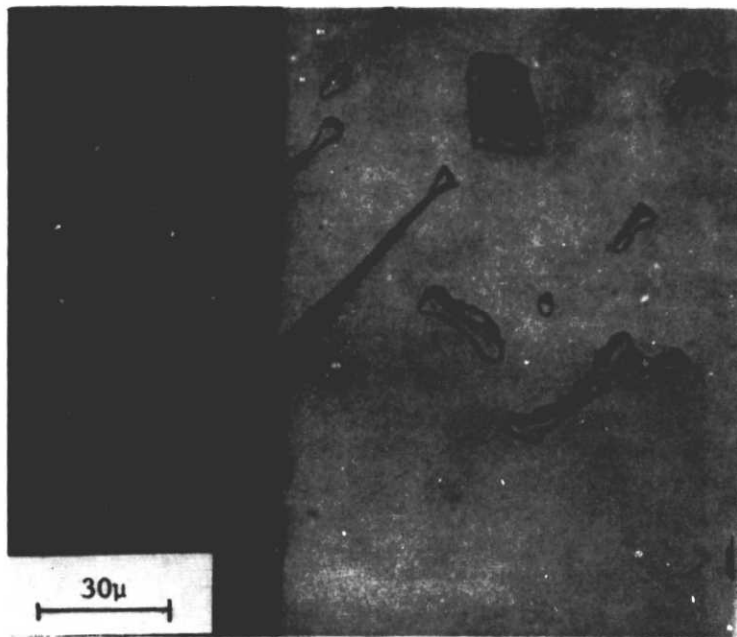
A



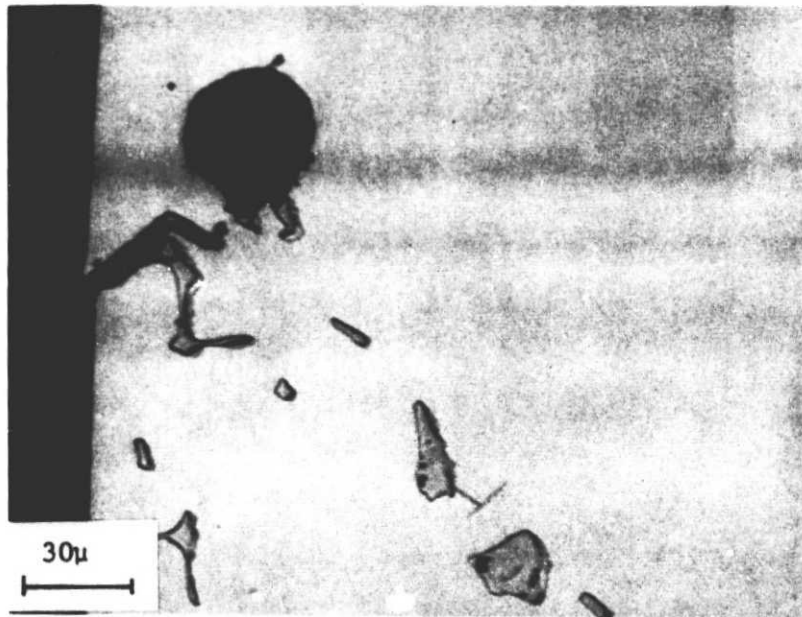
B

Fig. 13. Increasing magnification SEM fractographs showing micropores at the crack initiation site. Specimen FF23.

ORIGINAL FIGURE
OF POOR QUALITY



A



B

Fig. 14. Photomicrographs showing possible Stage I initiation at carbides. Specimen FF23.

ORIGINAL PAGE 17
OF POOR QUALITY

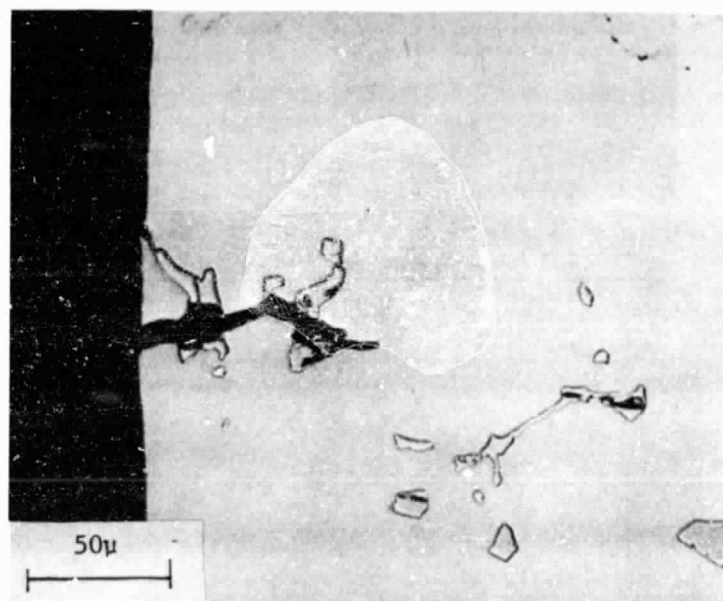
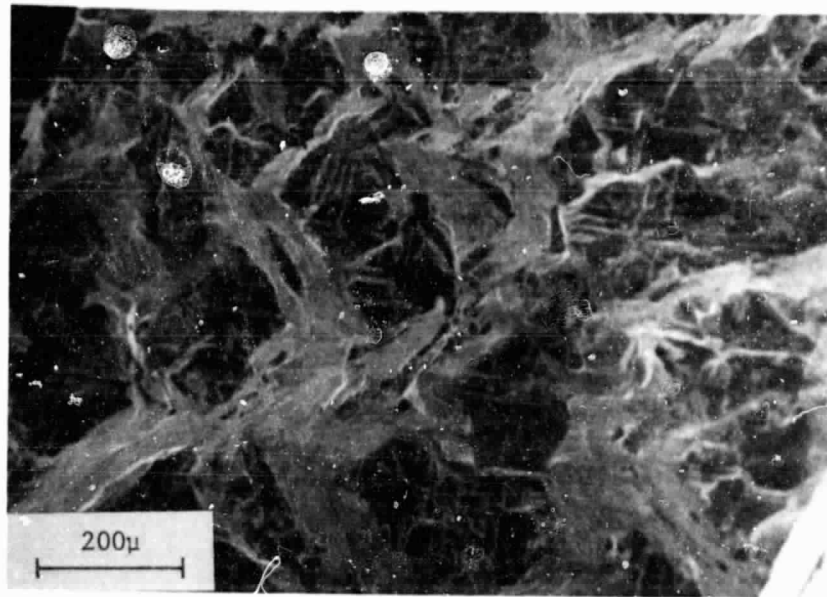
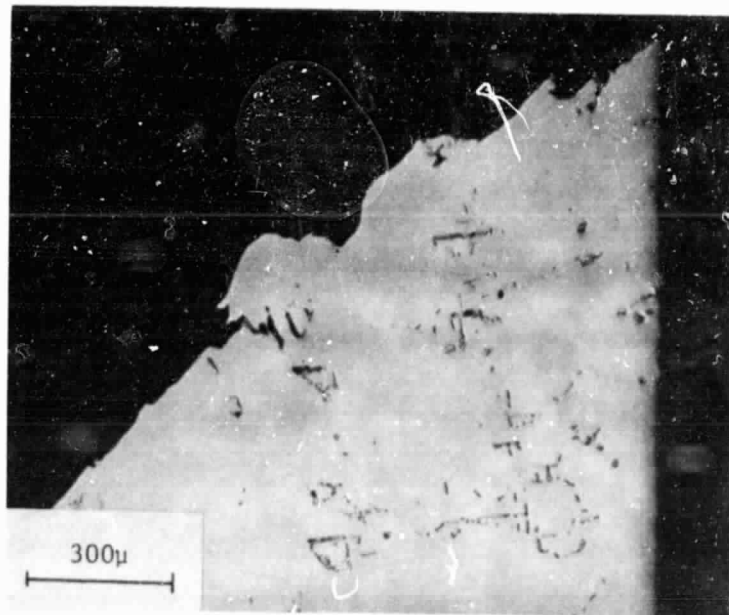


Fig. 15. Photomicrograph showing possible initiation at "cracked" carbides. Specimen FF43.



A



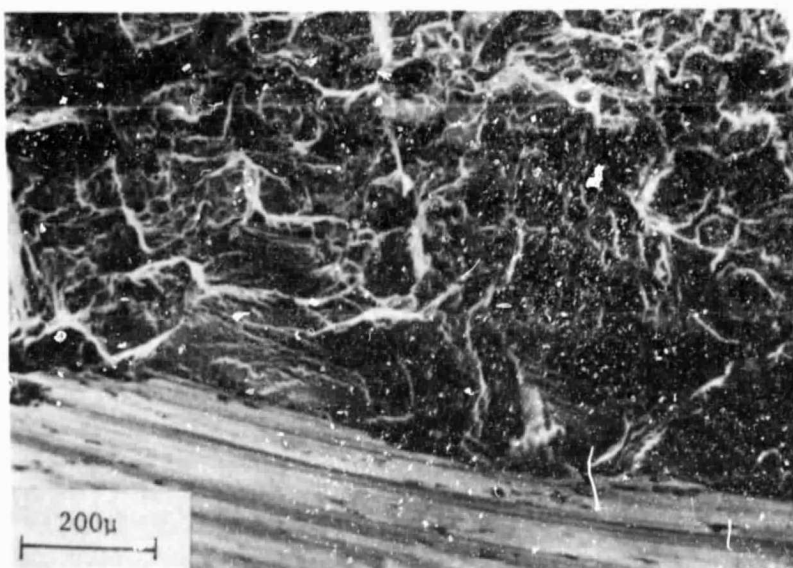
B

Fig. 16. Final tensile failure mode. A) SEM fractograph showing the dual nature of the crack. Smooth, lighter areas correspond to the octahedral shear planes, while darker, rough areas correspond to the dendrite boundaries (Note carbide pattern). B) Photomicrograph of the same specimen showing the shear plane fracture at about 45° to the tensile axis. Specimen FF23.

ORIGINAL PAGE IS
OF POOR QUALITY



A



B

Fig. 17. Slip traces on specimen surface due to shear on a single octahedral p'ane. A) Photomacrograph, Specimen FF43. B) SEM fractograph, same specimen.

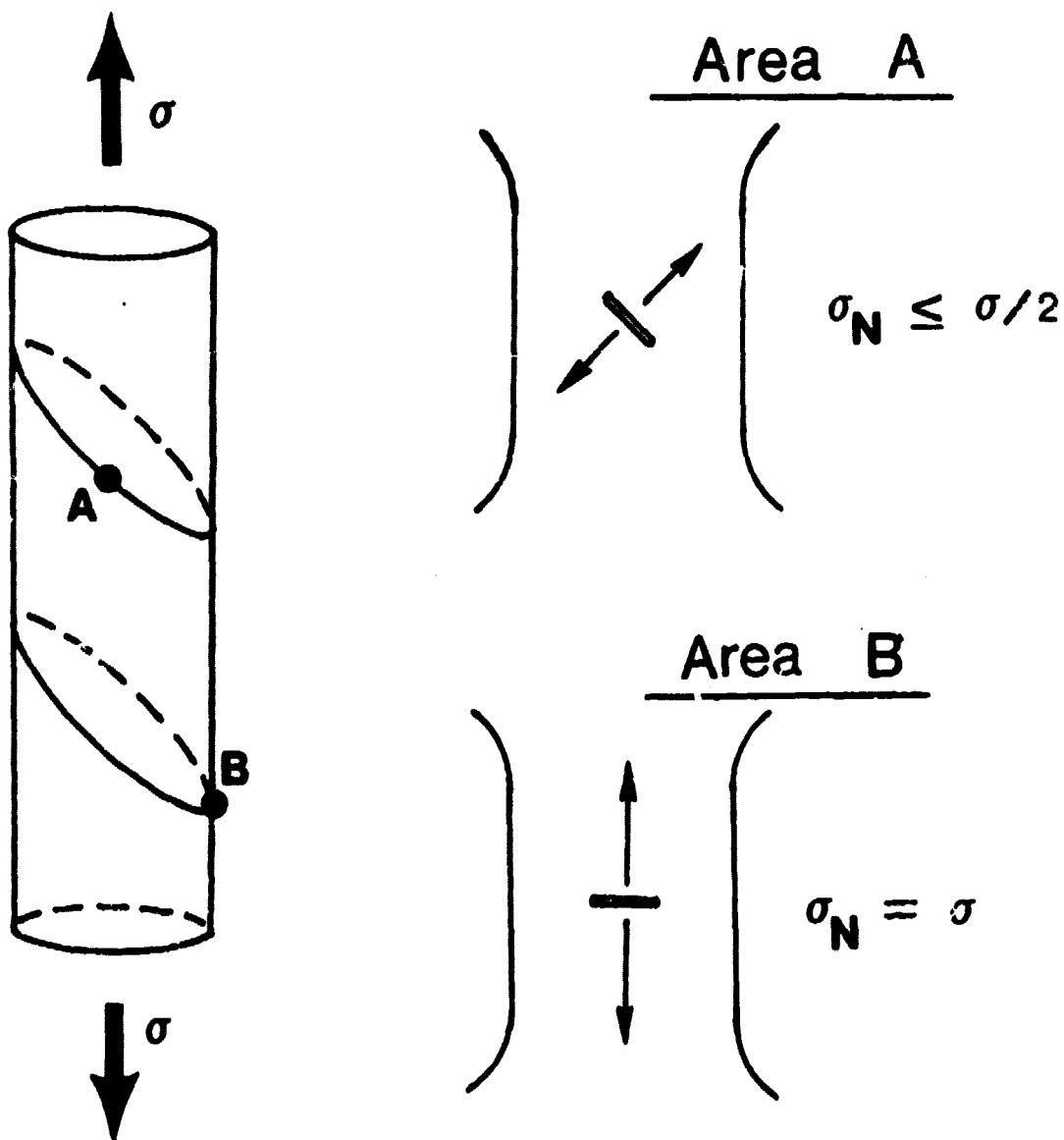


Fig. 18. Stress diagram illustrating why the fatigue crack initiation is at a consistent site on the specimen surface (Area B) in single slip orientations at 760°C.

ORIGINAL PAGE IS
OF POOR QUALITY

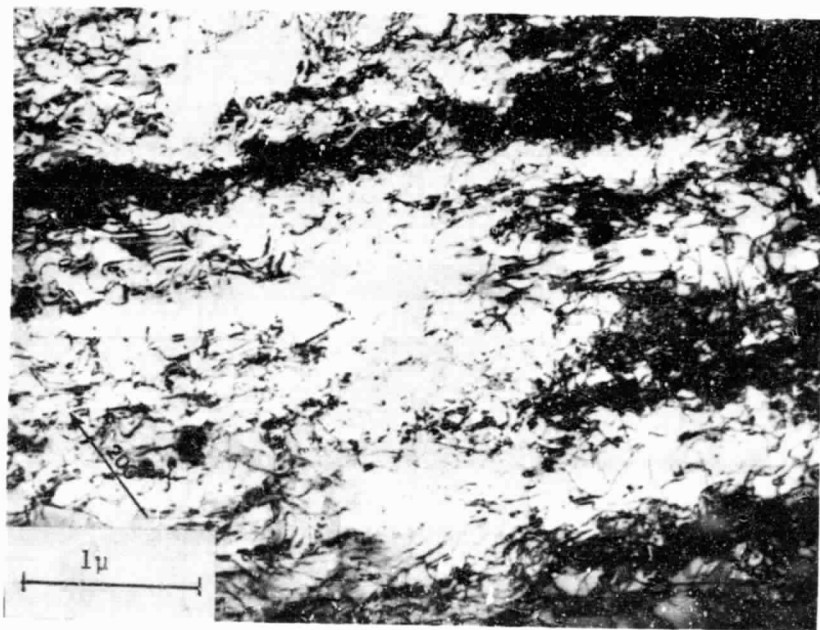
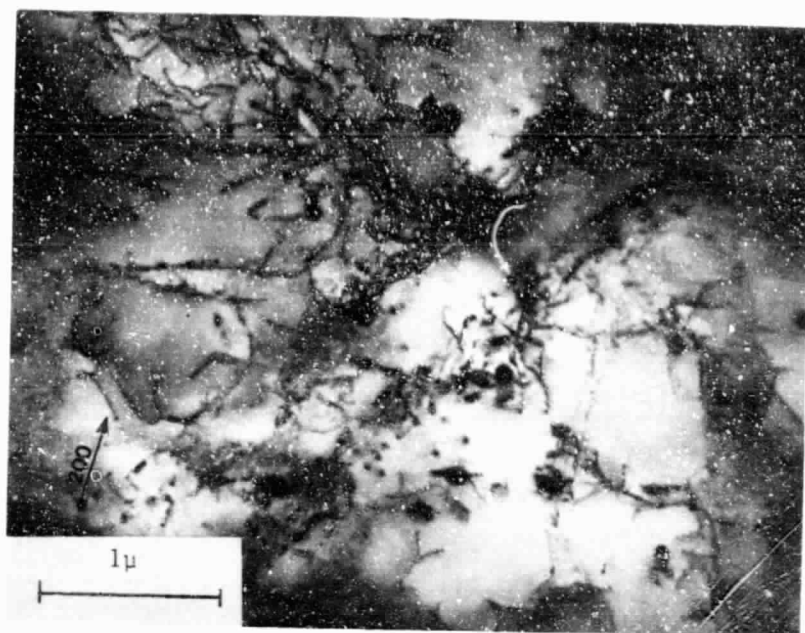
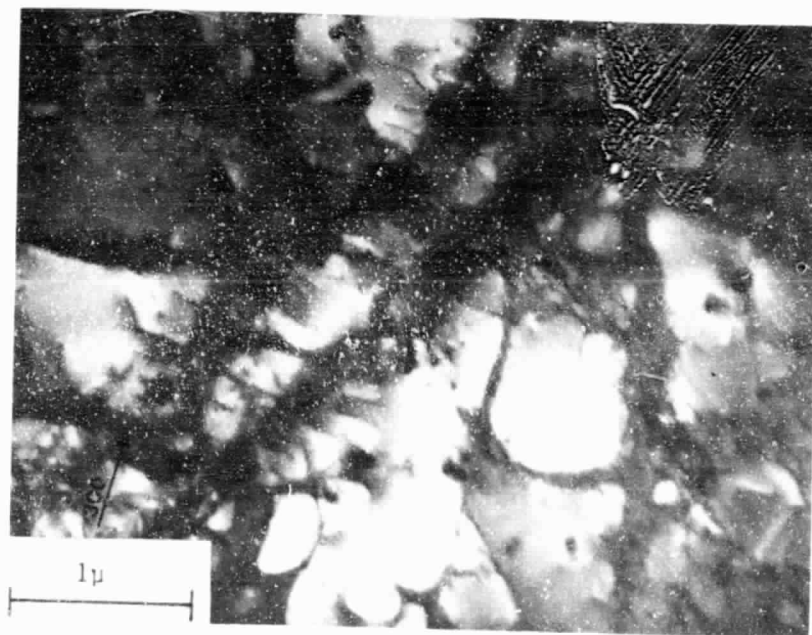


Fig. 19. BF TEM micrograph of deformation microstructure in a single slip orientation at 760°C. A) Specimen FF23. Note parallel dislocation bands.



A



B

Fig. 20.

TEM micrographs of slip bands in a multiple slip orientation at 760°C. Specimen 27, which was interrupted after 5 cycles. A) BF showing two parallel slip bands, and a 3rd (at left) intersecting at an angle. B) CDF of the same area. Note some dislocations in the γ' . Due to tilt constraints, the bands could not be brought into the "edge-on" condition to determine whether or not the γ' was being sheared.

ORIGINAL PAGE IS
OF POOR QUALITY

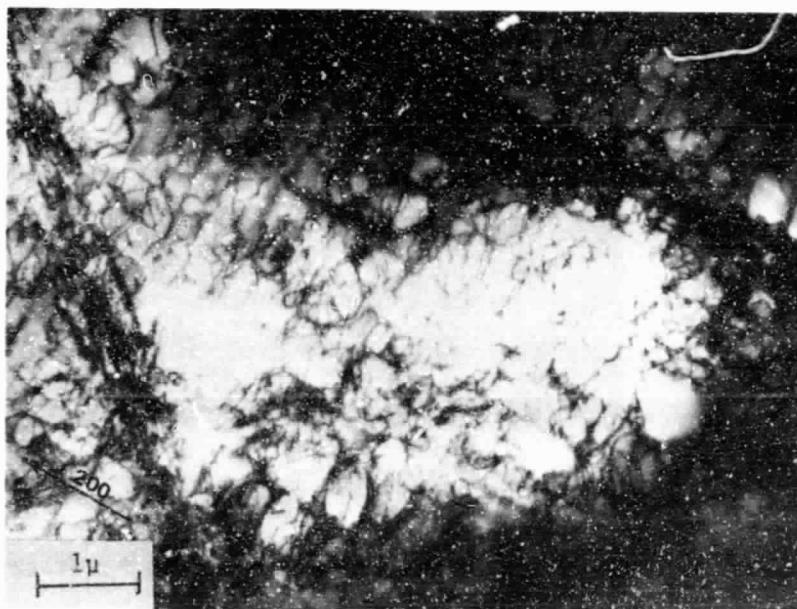


Fig. 21. BF TEM micrographs of specimen FF27 (Figure 23) showing three intersecting slip bands, and a high concentration of dislocations that were not in a band structure.

Table III

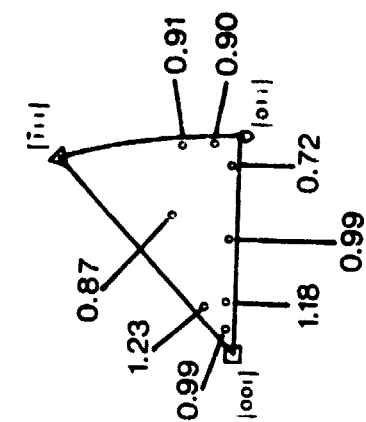
Experimental Data - 870°C

Specimen Number	E (20°C), GPa	E (870°C), GPa	$\Delta\epsilon_p$, %	$\Delta\epsilon_t$, %	$\Delta\sigma$, MPa	σ_m , MPa	N_f^2
34	120	96	0.091	0.99	862	59	1856
48 ¹	117	92	0.110	1.18	986	47	1003
51	110	87	0.100	1.23	986	47	1501
21 ¹	247	185	0.100	0.72	1150	93	630
46	200	150	0.110	0.90	1190	82	484
29	165	121	0.098	0.99	1080	24	1502
20	199	137	0.098	0.87	1060	-34	859
39	174	136	0.103	0.91	1100	115	552

¹Due to an experimental error, Specimens FF48 and FF21 were cycled at a positive mean strain of approximately 0.10%

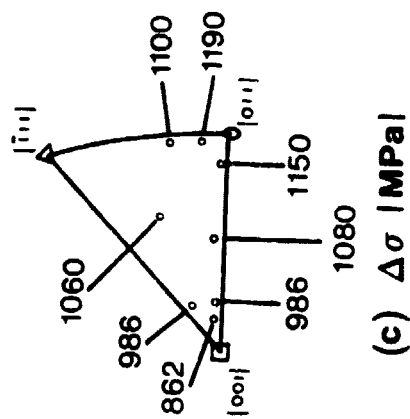
² N_f defined as total failure or a 10% drop in tensile load.

ORIGINAL FIGURE
OF POOR QUALITY

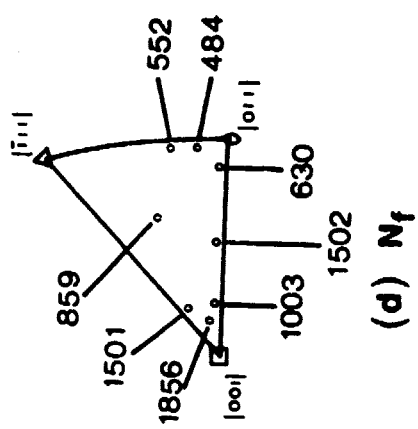


(a) $\Delta\epsilon_p$ %

(b) $\Delta\epsilon_t$ %



(c) $\Delta\sigma$ MPa



(d) N_f

Fig. 22. 870°C experimental data.

ORIGINAL 1-10-77
OF POOR QUALITY

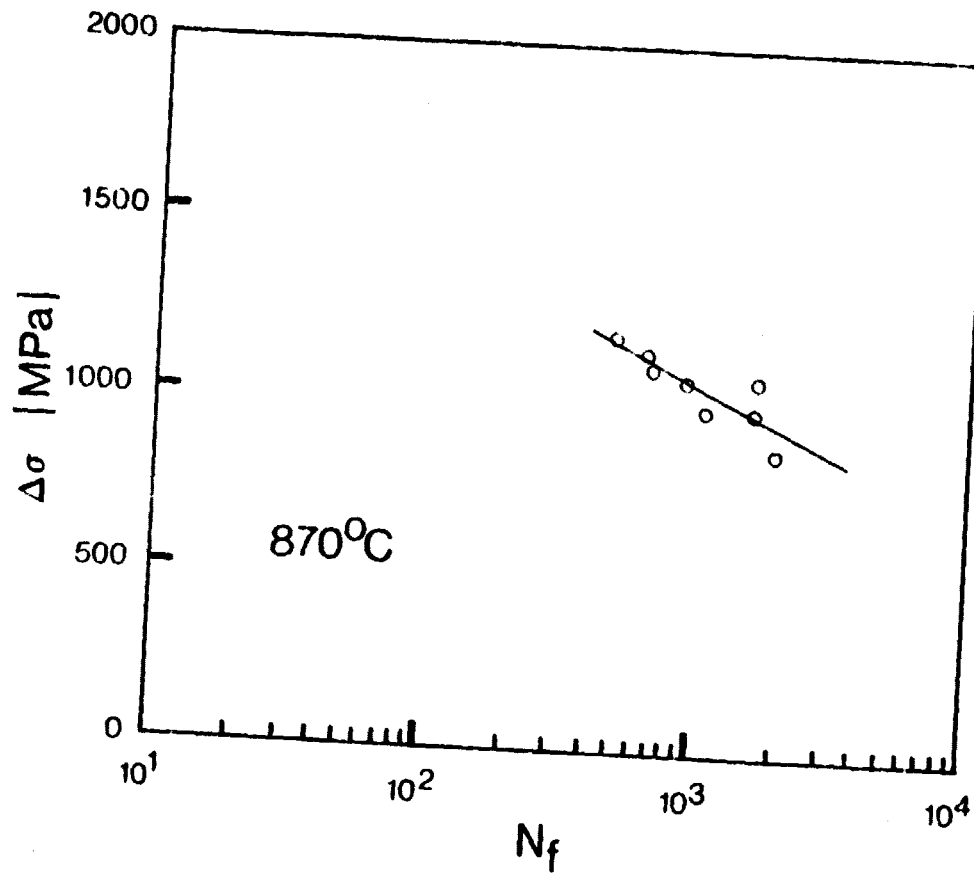


Fig. 23. $\Delta\sigma$ vs. N_f at 870°C.

ORIGINAL PAGE IS
OF POOR QUALITY

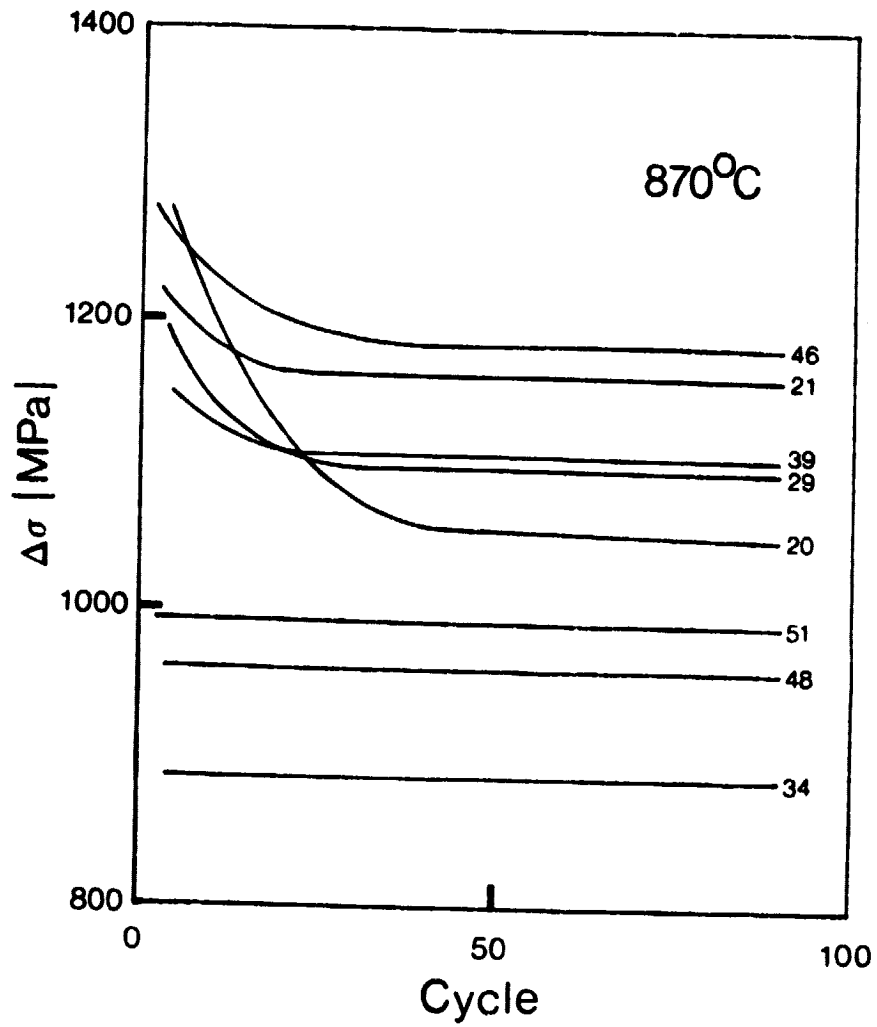
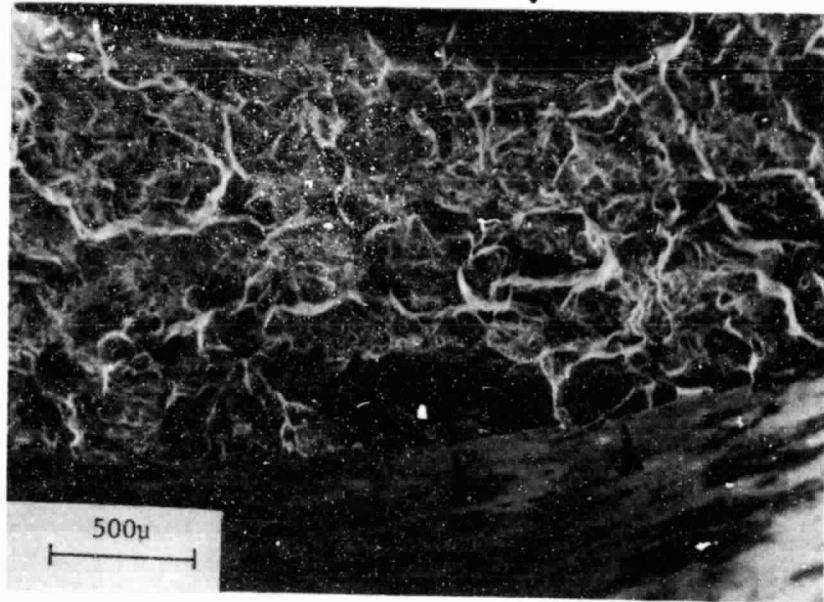
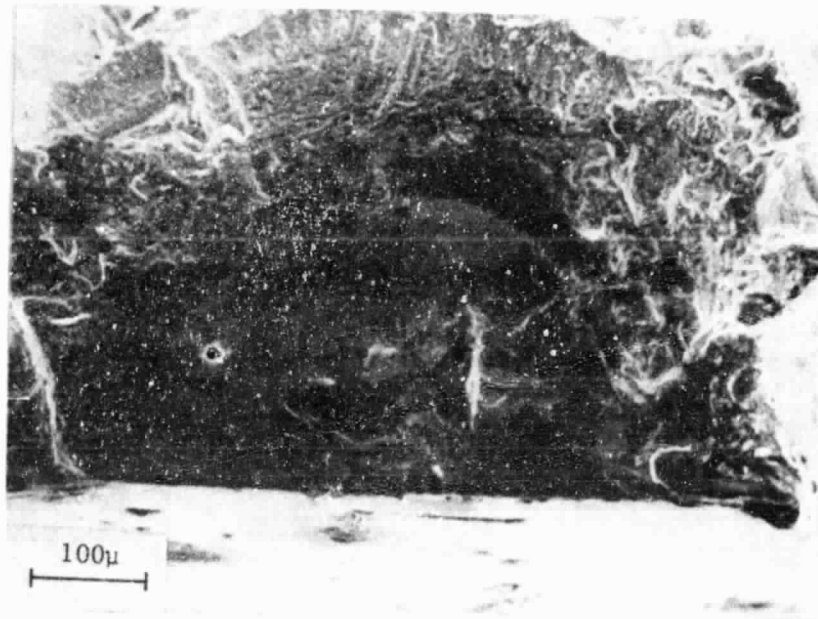


Fig. 24. Initial cyclic stress response at 870°C. The bottom three orientations are near (001).

ORIGINAL
OF POOR QUALITY



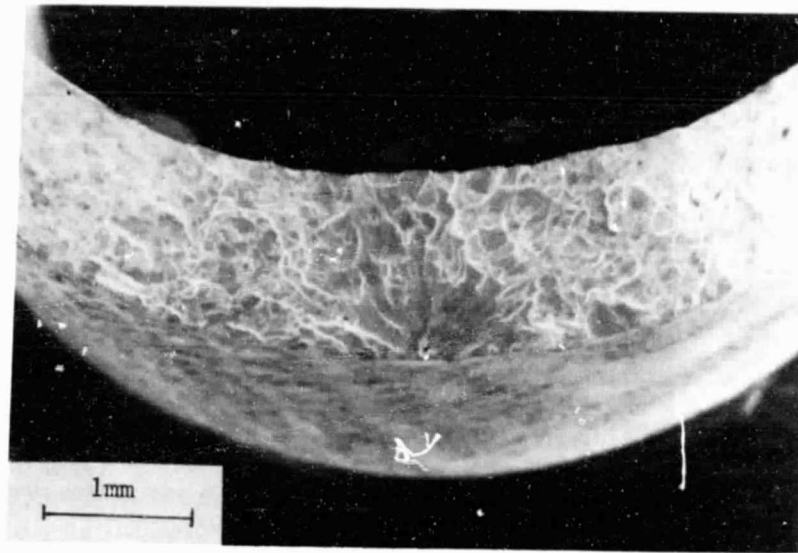
A



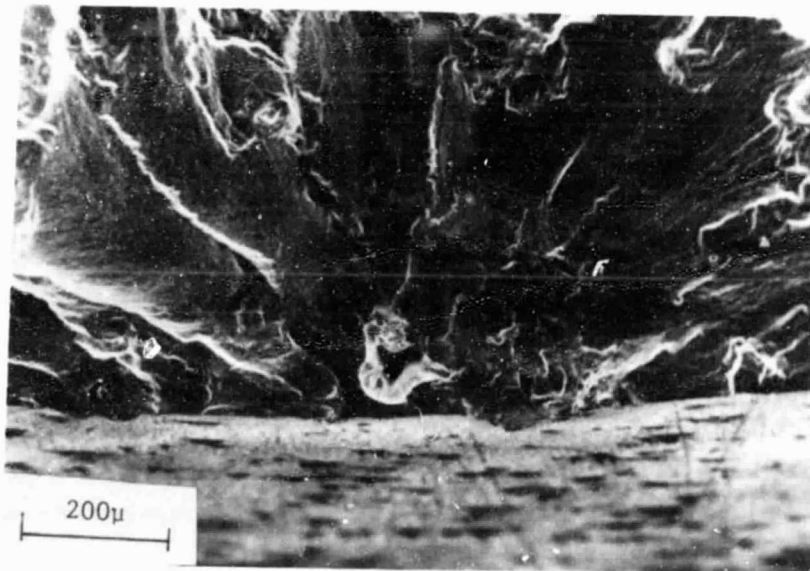
B

Fig. 25. Increasing magnification SEM fractographs showing smooth initiation zones and clamshell pattern in near (001) orientations at 870°C. Note 3 distinct origins (arrows) in top photo. Specimen FF34, low modulus.

ORIGINAL FILED
OF POOR QUALITY



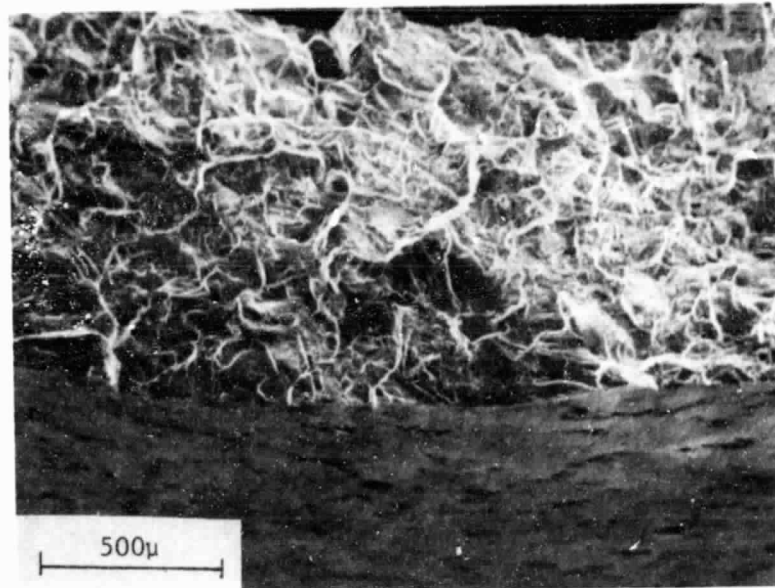
A



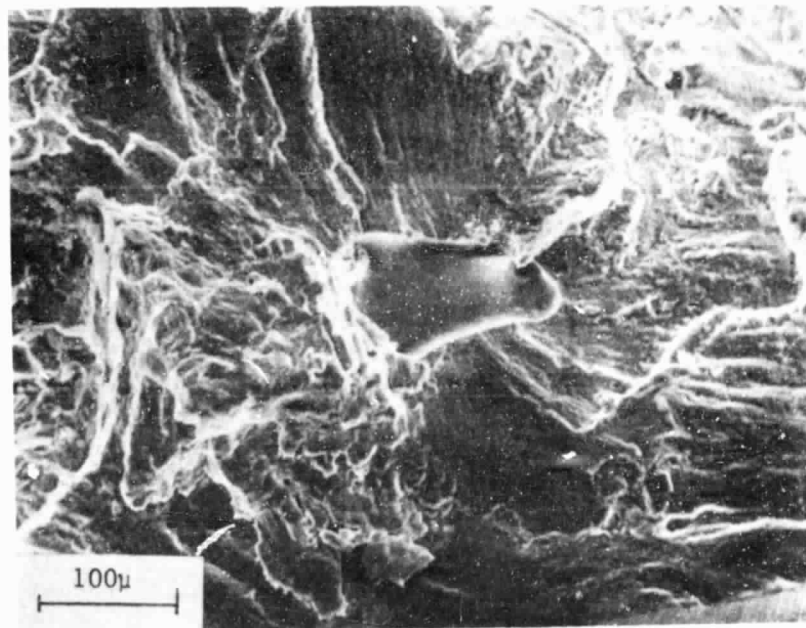
B

Fig. 26. Increasing magnification SEM fractographs showing initiation at a micropore, and a rougher initial propagation zone. Specimen FF29, intermediate modulus.

ORIGIN
OF POOR Q



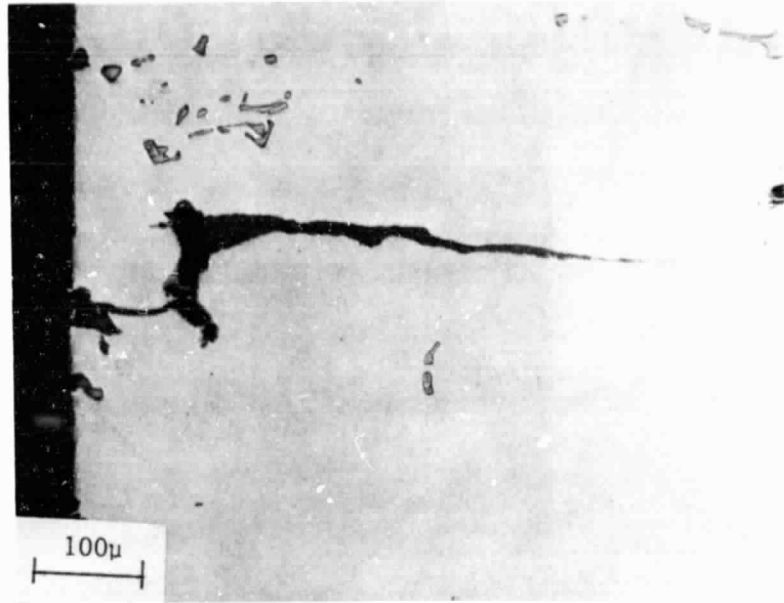
A



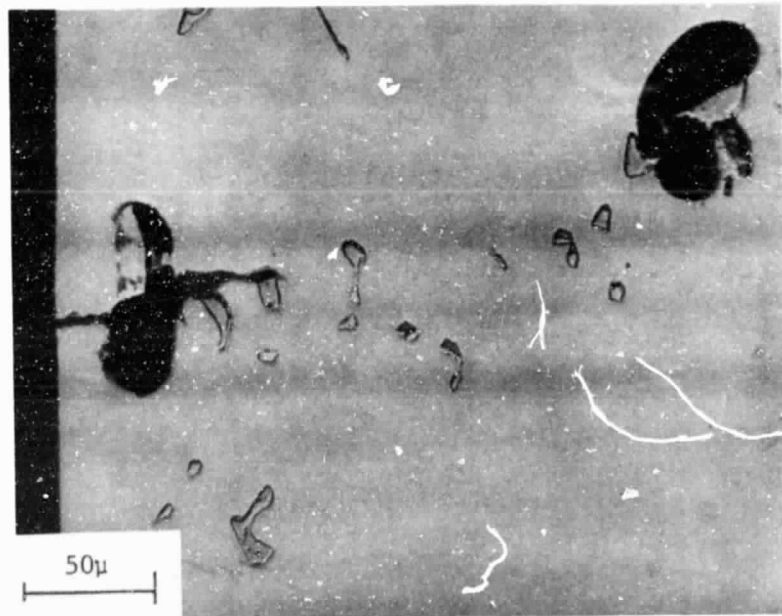
B

Fig. 27. Increasing magnification SEM fractographs showing initiation at a micropore, and a highly textured initial propagation zone. Specimen FF21, high modulus.

ORIGINAL PAGE IS
OF POOR QUALITY

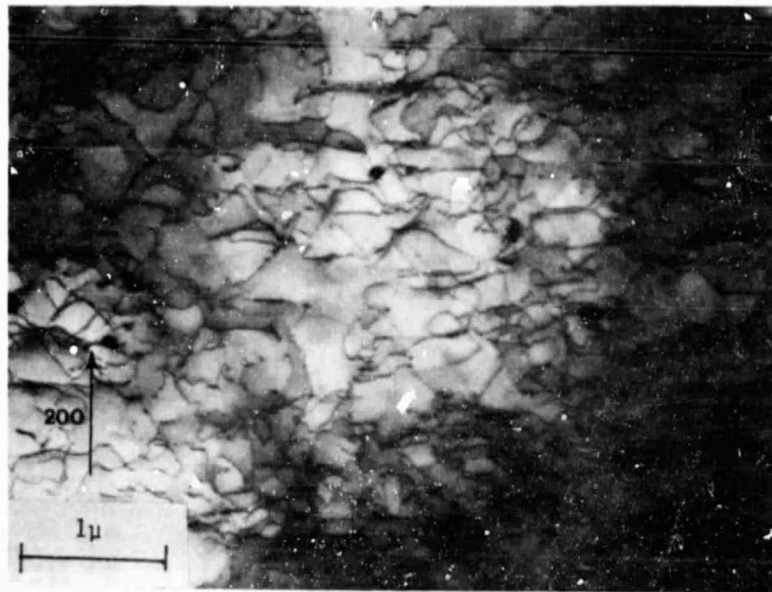


A

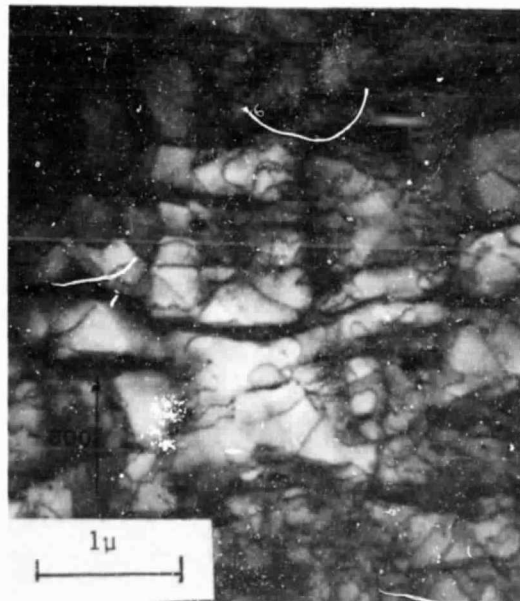


B

Fig. 28. Photomicrographs showing possible crack initiation at micropores. A) Specimen FF39. B) Specimen FF34.

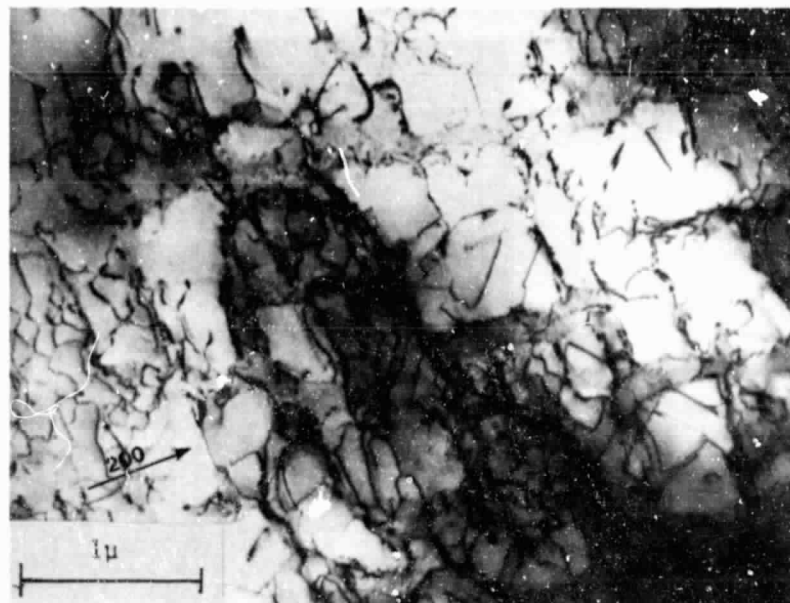


A

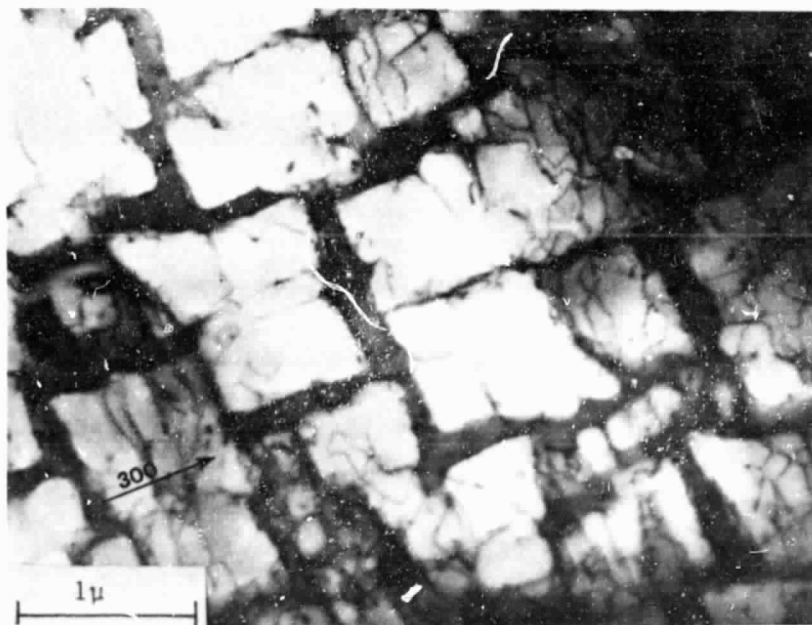


B

Fig. 29. TEM micrographs of deformation structure after testing at 870°C. Specimen FF21. A) TF showing wavy dislocation structure. B) CDF showing high concentration of dislocations in the γ' .

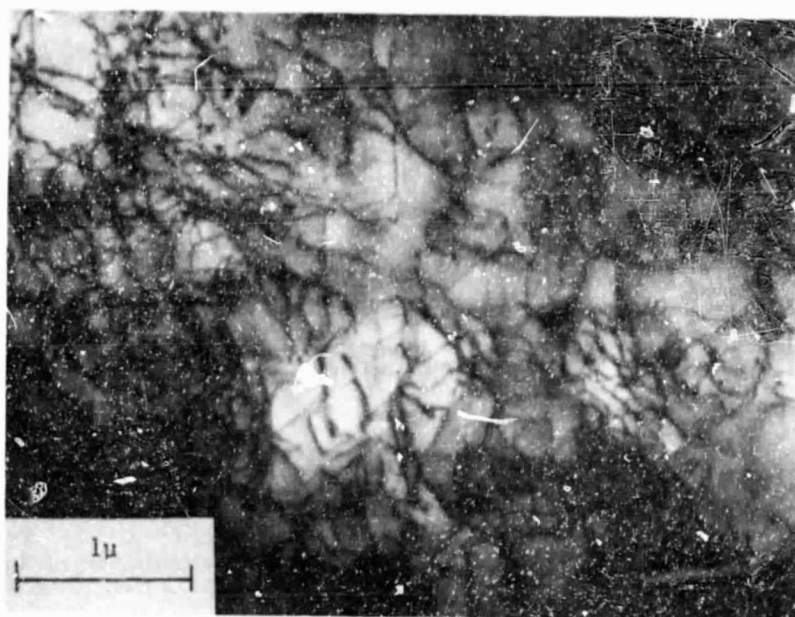


A

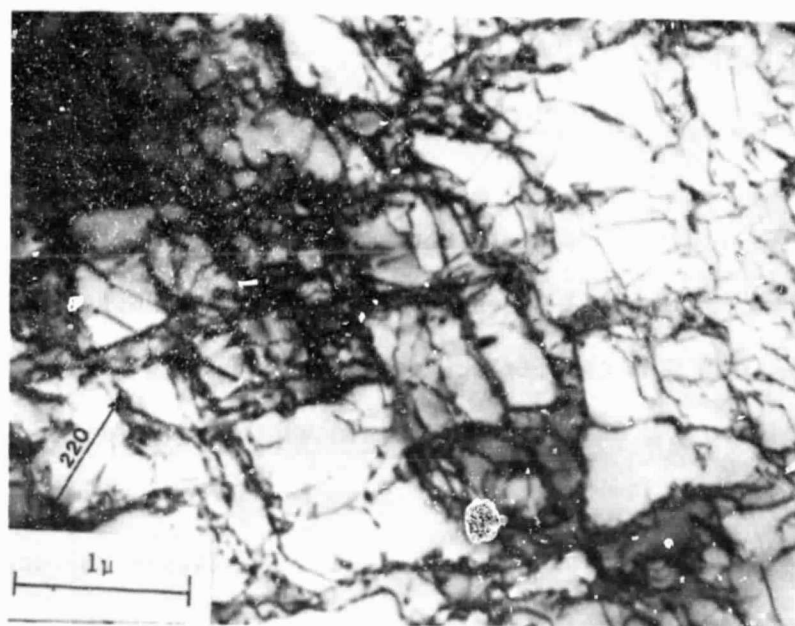


B

Fig. 30. TEM micrographs, Specimen FF43. A) BF. B) CDF of same area.



A



B

Fig. 31. TEM micrographs illustrating the similarity of the deformation structures in different orientations. A) Specimen FF21. B) Specimen FF48.

Appendix A

Procedure for Determining the Burgers Vector and Slip Plane

Symbols: \underline{g} - Diffraction vector joining the diffracted beam and the transmitted beam.

\underline{b} - Burgers Vector

\underline{u} - Line direction

From diffraction theory, a dislocation will be invisible under the two-beam conditions that satisfy the equation $\underline{g} \cdot (\underline{b} \times \underline{u}) = 0$. Residual dislocation contrast will result if $\underline{g} \cdot \underline{b} = 0$. Therefore, the burgers vector of a dislocation can be determined when two of these conditions are found.

The line direction of a dislocation can be determined by measuring the angle θ between a known direction (the \underline{g} vector) and the apparent (2-dimensional) line direction for three conditions.

Unless the dislocation is of a pure screw nature, \underline{b} and \underline{u} will lie on the same plane, defined as the slip plane.

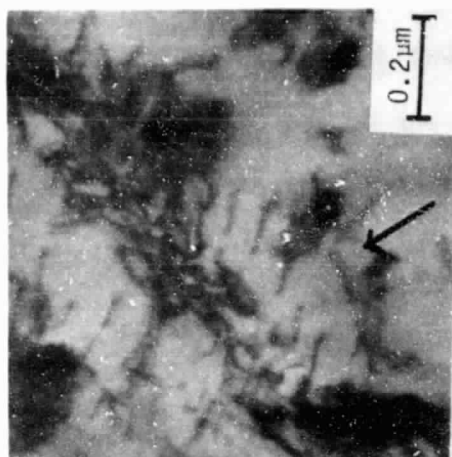
Example

The slip band in Specimen FF27 (Figure 23) was documented under 5 different two-beam conditions (Figures A1-A5). Two observed dislocations are present under three of these conditions (A1-A3), but disappear under the two other conditions (A4,A5). The two invisible diffraction conditions are: $\underline{g}_1 = (1\bar{1}1)$ and $\underline{g}_2 = (200)$. The burgers vector is defined as $\underline{g}_1 \times \underline{g}_2$, or (011) .

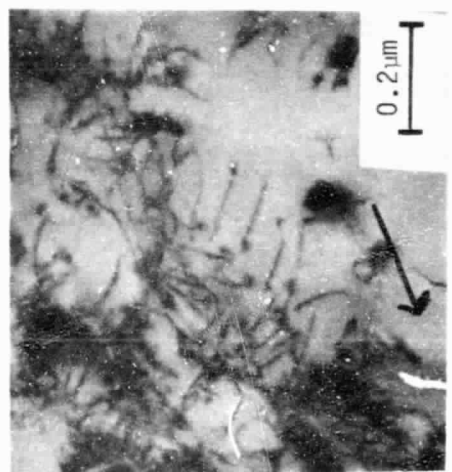
The apparent line direction was measured for the other three

diffraction conditions. The only direction that satisfies all three conditions (within experimental error) was $\underline{u} = (010)$.

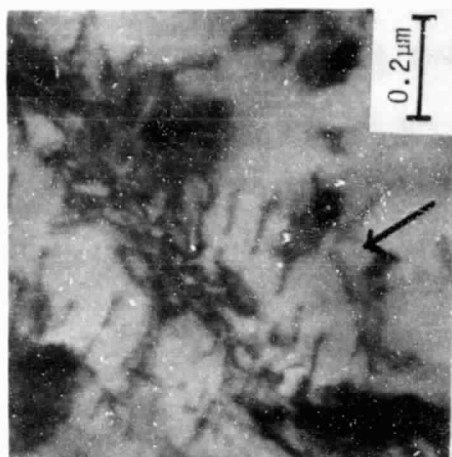
Since $\underline{b} \neq \underline{u}$, the dislocation is not pure screw, and the slip plane is defined by $\underline{b} \times \underline{u} = (100)$. These dislocations are therefore of the type $a/2 [011] (100)$.



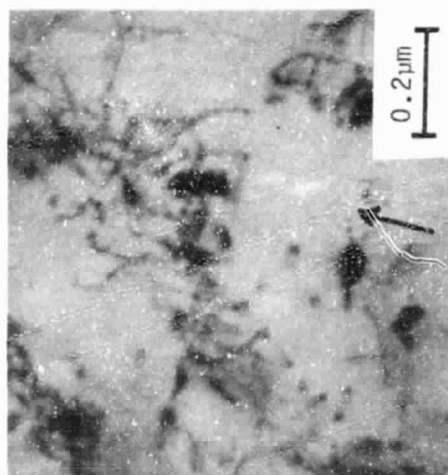
(a) $g = 020$



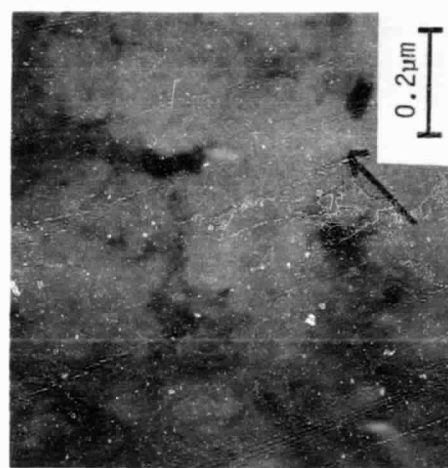
(b) $g = \bar{2}20$



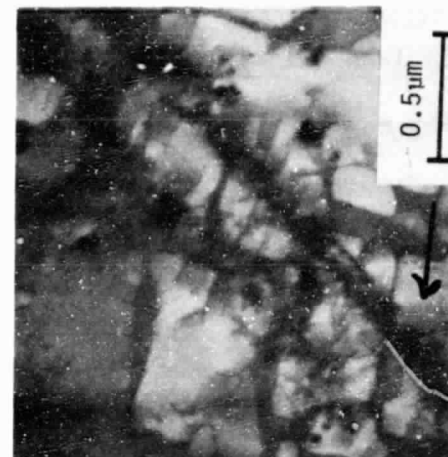
(c) $g = 220$



(d) $g = 200$



(e) $g = \bar{1}\bar{1}1$



(f) $g = 030$

Fig. A1. TEM micrographs illustrating the dislocation analysis technique. (a) - (e) are BF micrographs of the same area under different operating reflections. (f) is a lower magnification CDF of the same area.